DR. LUCÍA GUERRA (Orcid ID : 0000-0002-4019-1847)
DR. DANIEL ARIZTEGUI (Orcid ID : 0000-0001-7775-5127)

Article type : Original Article

Microstratigraphy and palaeoenvironmental implications of a Late Quaternary high-altitude lacustrine record in the subtropical Andes

LUCÍA GUERRA[1,2,3], MATEO A. MARTINI[3], HENDRIK VOGEL[4], EDUARDO L. PIOVANO[3], IRKA HAJDAS[5], RICARDO ASTINI[3], ANTOINE DE HALLER[2], ANDREA MOSCARIELLO[2], JEAN-LUC LOIZEAU[6] and DANIEL ARIZTEGUI[2]

[1]Departamento de Ciencias Ecológicas, Facultad de Ciencias. Universidad de Chile, Las Palmeras 3425, Ñuñoa, Santiago, Chile (E-mail: luciaguerra83@gmail.com / lguerra@unc.edu.ar)

[2]Department of Earth Sciences, University of Geneva, Rue des Maraichers 13 CH-1205 Geneva, Switzerland.

[3]CICTERRA, CONICET- Universidad Nacional de Córdoba, Av. Vélez Sarsfield 1611, X5016GCA, Córdoba, Argentina.

[4]Institute of Geological Sciences & Oeschger Centre for Climate Change Research, University of Bern, Baltzerstrasse 1+3 3012 Bern, Switzerland.

[5]Laboratory of Ion Beam Physics, ETH Zurich, Otto-Stern-Weg 5, 8093 Zurich, Switzerland.

This article has been accepted for publication and undergone full peer review but has not been through the copyediting, typesetting, pagination and proofreading process, which may lead to differences between this version and the Version of Record. Please cite this article as doi: 10.1111/SED.13004

[6]Department F.A. Forel for Environmental and Aquatic Sciences, University of Geneva, Uni Carl Vogt - 66, boulevard Carl-Vogt, Geneva, Switzerland.

Associate Editor – Lauren Birgenheier

Short title – High-altitude lacustrine microstratigraphy

ABSTRACT

High-mountain lake records in semiarid foreland settings, such as the central Andes of North-western Argentina, are highly restricted and often deprived of well-preserved microstratigraphic information to analyze palaeoenvironmental changes and their causes, particularly for periods prior to the Last Glacial Maximum. Laguna La Salada Grande (23ºS/65ºW, 4063 metres above sea-level) is a closed shallow lake located at Cordillera Oriental, North-western Argentina with a unique depositional record, including geomorphic and stratigraphic evidence of palaeoenvironmental changes since the Late Pleistocene. In order to understand the depositional dynamics of this mountain lacustrine system at different timescales, limnogeological multiproxy analyses together with a radiocarbon and ^{210}Pb-based chronology were applied on massive and laminated sediments from La Salada Grande. Laminated deposits were further analyzed using novel sub-centimetric mineralogical, textural and geochemical automated methods (including a combination of micro-X ray fluorescence and Quantitative Evaluation of Minerals by Scanning Electron Microscopy (QEMSCAN®). Thick laminated microfacies at the beginning of the sequence record a deep and organic matter productive palaeolake prior to *ca* 34 ka (1 ka = 1000 years before 1950), that changed into a highly fluctuating shallower-palaeolake with frequent detrital influxes after *ca* 34 ka. Microstratigraphy of the coarser-grained detrital laminae between 31 ka and 25 ka reveals irregular and probably sub-centennial high-energy discharge events, pointing to convective atmospheric activity as the main trigger. After *ca* 21 ka the lake evolved to deeper water-level conditions resulting in fine-grained deposits with limited delivery of coarse-grained sediments, followed by an abrupt lake level drop and incision. The multi-millennial palaeoenvironmental reconstruction of La Salada Grande, and its correlation with other palaeoclimate records, shows a close link between the lacustrine depositional processes and

palaeoclimate changes associated to the South American summer monsoon dynamics. This multifocal research in such an understudied environment provides key knowledge about lacustrine functioning and discharge events-climate interactions of mountain lakes of semi-arid climates.

Keywords Cordillera Oriental, foreland lakes, high-frequency events, lamination, Late Pleistocene, North-western Argentina, QEMSCAN, semi-arid environment.

INTRODUCTION

The sedimentological functioning and deposits of foreland closed lakes in arid and semi-arid areas is poorly understood (Cohen *et al.*, 2015), and detailed microfacies studies of their sediments are scarce. Lacustrine deposits record a combination of local site-specific changes related to the depositional environment and catchment hydrology as well as the influence of regional-scale climate variations and their impact on the environment at different temporal scales. Detailed information can be found in laminated lake sediments (for example, varves) which can form in a wide spectrum of settings associated with changes on lake stratification, algal blooms, detrital supply, chemical or bio-induced precipitation, or a combination of these processes (Hardie *et al.*, 1978; Kemp, 1996; Renaut & Gierlowski-Kordesch, 2010; Zolitschka *et al.*, 2015). The best chances of preservation of these laminated sediments are in deep, stratified and wind-protected lakes with high sedimentation rates (Kemp, 1996; Brauer, 2004; Zolitschka *et al.*, 2015). Contrastingly, in ephemeral lacustrine systems from arid and semi-arid foreland areas, where wind-erosion and alluvial deposition are prominent, rhythmically laminated deposits are usually restricted.

An increasing number of studies are using micromorphology and microfacies analysis on laminated lacustrine deposits to enlighten about the processes behind the laminae formation (e.g. Mangili *et al.*, 2005, van der Meer & Menzies, 2011; Martin-Puertas *et al.*, 2012, 2014; Schlolaut *et al.*, 2014; Neugebauer *et al.*, 2015, 2016; Ben Dor *et al.*, 2019). To this end, automated geochemical determinations and image analyses have been successfully applied in microscopic litho-facies and chemo-facies in order to detect variations of clastic supply (e.g. Schillereff *et al.*, 2014), bottom oxygenation (e.g. Neugebauer *et al.*, 2018) and chemical precipitation (e.g. Neugebauer *et al.*, 2015). Additionally, high resolution microstratigraphy has been used for

developing cycle and event stratigraphic frameworks including recurrent floods and droughts (e.g. Gilli *et al.*, 2013; Schillereff *et al.*, 2014; Schlolaut *et al.*, 2014; Neugebauer *et al.*, 2015; Noble *et al.*, 2016), mass wasting events (e.g. Waldmann *et al.*, 2011), palaeoseismology and frequency of volcanic activity (e.g Wulf *et al.*, 2013), providing the basis for regional correlations (e.g. Alloway *et al.*, 2007). In combination with other automated techniques, quantitative evaluation of minerals by scanning electron microscopy (QEMSCAN), which was traditionally used for mining and oil industries, has been recently applied to mineralogical determinations of fine-grained sediments in environmental studies (e.g. Šegvić *et al.*, 2015; Amao *et al.*, 2016; Kenis *et al.*, 2020), although its use in Quaternary lacustrine microstratigraphy is still limited (Lynch *et al.,* 2015; Fagel *et al.*, 2021).

At high-elevation landscapes from the subtropical Andes of North-western Argentina, Quaternary palaeoclimate records are largely restricted as a result of high aridity coupled with geographical isolation and limited accessibility. Time-constrained palaeoenvironmental records in such extreme conditions are thus fundamental pieces to reconstruct climate behaviour in the past.

At present, the climate in the North-western Argentinean Andes is controlled by the South American Summer Monsoon (SASM) system (Zhou & Lau, 1998; Vera *et al.*, 2006), which supplies most of the humidity during the austral summer months (Garreaud, 2009). For the Late Pleistocene, information regarding the past SASM activity at its south-western influence area has been studied through glacial geomorphology (e.g. Zech *et al.*, 2009; Martini *et al.*, 2017a; D'Arcy *et al.*, 2019; Palacios *et al.*, 2020), fluvial and mass wasting deposits (e.g. Trauth *et al.*, 2003; Schildgen *et al.*, 2016; Tofelde *et al.*, 2017), large salt-pans (e.g. López Steinmetz &Galli, 2015), and shallow lake, playa-lake and wetland records (e.g. Grosjean *et al.*, 1997, 2001; Valero-Garcés *et al.*, 2000; Schäbitz *et al.*, 2001; Lupo *et al.*, 2006; Schittek *et al.*, 2015, 2016; Torres *et al.*, 2016; McGlue *et al.*, 2017; Kock *et al.*, 2019; Hooper *et al.*, 2020). Because a large part of the region has been glaciated during the Late Pleistocene (Zech *et al.*, 2009; Martini *et al.*, 2017a), most of the mountain palaeoclimatic records only provide information of the time after the deglaciation (Schäbitz, 2001; Zech *et al.*, 2009; Coppo, 2015; Hooper *et al.*, 2020). Furthermore, small, ephemeral, endorheic lakes settled within this high-relief and semi-arid region, usually impedes the formation and preservation of long-term laminated deposits, and thus available records are not usually optimal for high-resolution studies. Among the sparse shallow lakes found in the high mountains of North-western Argentina, Laguna La Salada Grande (LSG) comprises a closed, relatively standing water body that was outside the glacial influence during the Last

Glacial Maximum (LGM, 26.5 to 19 ka; Clark *et al.*, 2009), presenting a remarkable long sedimentological record, which extends back, at least, to the Late Pleistocene. La Salada Grande lacustrine deposits include finely laminated sections which permit palaeoenvironmental studies with a micrometric level of detail.

In this work, a multiproxy approach, including geochemical and petro-physical analyses, is applied to investigate the major sedimentological changes that occurred in LSG under contrasting hydrological conditions. Microstratigraphy is refined through automated techniques including scanning X-ray fluorescence (XRF), micro-XRF combined with microscopic observations in thin sections. In addition, quantitative evaluation of minerals by scanning electron microscopy (QEMSCAN) maps are applied to examine the mineralogy, texture and fabric in laminated microfacies. This microstratigraphic approach enhances the knowledge of detailed depositional dynamics under changing climates in semi-arid high-mountain-lakes located at foreland areas. A special focus is set on the last part of the relatively warmer interstadial (Marine Isotope Stage 3, MIS 3, 57 ka to 29 ka) towards the transition to MIS 2 during the last glacial cycle, where a high-frequency event stratigraphy is introduced for this high-altitude system. After debating the chronology of the record, the LSG long-term palaeoenvironmental reconstruction (MIS 3 to the present) is discussed and inserted into a regional and global context, linking the lake major changes to the past SASM activity.

STUDY AREA

Laguna La Salada Grande [23° 7' 48.3" S, 65° 11' 31.9" W, 4063 metres above sea level (m a.s.l.)] develops immediately west of the line of major heights in the doubly-vergent Cordillera Oriental belt (**Fig. 1A** and **B**) atop of thick-skinned thrusts that unroofed Late Proterozoic basement (meta-graywackes) and early Cambrian quartz arenites cover (Gonzalez *et al.*, 2003). The Laguna La Salada Grande basin can be classified as an underfilled basin (cf. Carroll & Bohacs, 1999) linked to the Andean hinterland-top wedge area (Cohen *et al.*, 2015), where restricted and relatively small endorheic depressions develop. Under present-day conditions, LSG seems largely as a playa-lake system (cf. Arche, 2008), although satellite images show the lake is covered by water in most of the scenes of the last decade (2010 to 2018), except during 2018 when it showed a moment of almost total drought, revealing a persistent water coverage.

Laguna La Salada Grande is a shallow (*ca* 1 m maximum depth when sampled in 2016), closed, alkaline (pH>8) lake with high total dissolved solids (oligohaline, 8 g l^{-1}) (**Fig. 2**). Current lake watershed covers an area of 13 km^2 with a maximum altitude of 4470 m a.s.l. A smaller playa, Laguna La Salada Chica (LSC), is located 1.5 km to the west of LSG, separated by a sill (**Fig. 2**). Laguna La Salada Grande has no permanent surficial water inflow and is fed by groundwater and ephemeral streams that dissect the terrain and activate during episodic summer storms.

The surrounding lake sub-environments are composed of a mudflat with clayey deposits and sparse saline efflorescence, and a main active delta in the western part of the lake (**Fig. 2A** and **B**). Vegetation around LSG is characterized by grasslands accompanied by perennial herbs and cushions, which are characteristic of the semiarid highlands in the Andes (Torres *et al.*, 2016). Geomorphic and stratigraphic evidence around LSG, such as terraces, a palaeodelta towards the south-east of the lake, gullies, a terrace scarp and different palaeoshorelines (**Fig. 2**), indicate that substantial hydrological changes occurred in the past. The highest palaeoshoreline is located 29 m above the current lake level and 24 m below the watershed spill-point elevation (4116 m a.s.l.; **Fig. 2A**), indicating that endorheic conditions prevailed throughout the LSG history.

Annual variability of the lake hydrology is linked to the SASM. During the beginning of the austral spring, the Intertropical Convergence Zone (ITCZ) moves southward and produces the onset of the SASM (Zhou & Lau, 1998; Vera *et al.*, 2006; de Carvalho & Cavalcanti, 2016), which reaches its mature phase between December and March generating a strongly seasonal precipitation in the study area (>75% of total). Moisture is carried by east-north-easterly winds that produce a sharp orographic precipitation gradient as a consequence of the Cordillera Oriental barrier to the moisture flow (Bianchi & Yañez, 1992; Viale *et al.*, 2019). This effect reduces the precipitation from 1200 mm $year^{-1}$ in the eastern lowlands to less than 400 mm $year^{-1}$ above 4000 m a.s.l. in the mountain area of LSG at 23°S (Bianchi & Cravero, 2010) (**Fig. 1A**). During the austral winter (dry season) the ITCZ moves northward, the SASM vanishes, and dry westerlies prevail in the region. The regional altitude of the 0°C isotherm (freezing level) is ~5000 m a.s.l. overlapping with the highest ranges at this part of the Cordillera Oriental (Martini *et al.*, 2017b). The estimated mean annual temperature at LSG is 6.6°C, based on an interpolation of *in situ* data from a nearby site (Martini *et al.*, 2017b). During winter, the temperature remains below 0°C for short periods of time and produces sporadic freezing of part of the lake water surface.

MATERIALS AND METHODS

Sedimentary logs, chronology and multiproxy processing

In April 2016, the general stratigraphy of outcrops correspondent to a gully, and of a terrace scarp located near the LSG (outcrops 1 to 3; **Fig. 2**) was inspected. From outcrop 3, a 15 cm thick sediment section (comprising a 7 cm thick volcanic ash deposit), was extracted by introducing a 2 cm width C-shaped plastic profile into an exposed cleaned vertical scarp of the terrace.

Two cores of 150 cm length, LSG1 and LSG2, were retrieved using a vibro-corer system (**Fig. 2B to D**). LSG1 core was recovered from the lake centre, until the drilling system was blocked by an impenetrable layer (**Fig. 2C**) whereas LSG2 core was recovered from the southern lake shore area (**Fig. 2D**).

Cores were stored in a 4ºC chamber (Centro de Investigaciones en Ciencias de la Tierra, CICTERRA, Córdoba, Argentina), then opened in two halves lengthwise and photographed (Department of Geology, University of Geneva, Switzerland). Volumetric magnetic susceptibility (MS, measured in SI units) was determined using a MS2E Bartington sensor (Bartington Instruments Limited, Witney, UK) at the University of Geneva with 0.5 cm resolution. A core description was made following the LacCore criteria (Schnurrenberger *et al.*, 2003) and different sedimentary units were identified according to the main lithological and physico-chemical properties observed in the sequence.

Six samples from LSG1 and LSG2 cores and one from the gully outcrop 1 (**Figs 2** and **3** – including bulk organic matter, carbonate and organic macro-remains), were selected for radiocarbon dating. Samples were pre-treated following methodology described by Hajdas (2008) and measured by accelerator mass spectrometry (AMS using the Mini Carbon Dating System (MICADAS, ETH, Switzerland) at the Laboratory of Ion Beam Physics, Zurich, Switzerland (Synal *et al.*, 2007). Ages were calibrated using the SHCal20 atmospheric curve (Hogg *et al.*, 2020). One post-bomb age was calibrated using the SH Zone1-2 (Southern Hemisphere Zone 1 and 2 compilation) calibration dataset (Hua *et al.*, 2013). The radiocarbon ages of the top sediments from both cores were compared with preliminary ^{210}Pb and ^{137}Cs radioisotope activity profiles (see Appendix S1 for methodology and results).

Continuous elemental composition (Al, Si, S, Cl, K, Ca, Ti, Mn, Fe, Zn, Rb, Sr, Zr and Ba) was determined on one half of each core using a non-destructive ITRAX core scanner (COX Analytical Systems, Mölndal, Sweden; Croudace *et al.*, 2006; University of Bern, Switzerland).

The measurements were performed with a Cr-tube, using an exposure time of 20 s, 30 kV voltage and 50 mA current. Measurement intervals varied between 5 mm for massive sediments, and 1 mm for finely laminated sections of the core. In the laminated sections, the number of positive excursions of X-ray fluorescence (XRF) selected elements and specific calculated ratios were counted using a 1 mm resolution. Positive peaks were contrasted against the high-resolution photographs.

A principal component analysis (PCA) was applied on the XRF data of the LSG1 and LSG2 cores to distinguish the main elemental associations. After eliminating anomalous results and removing an event layer corresponding to a tephra from the database, two principal components were calculated on standardized data using the centered log-ratios [ln (element intensity / geometric mean of range of elements)] or the log-element ratios between elements (Weltje & Tjallingii, 2007; Neugebauer *et al.*, 2018; Morlock *et al.* 2021).

Samples along LSG2 core were taken at irregular intervals (*ca* 3 to 10 cm), freeze-dried and powdered in an agate mortar and then examined using an elemental Perkin Elmer© analyzer (PerkinElmer Inc., Waltham, MA, USA), in order to analyze total C, N and S. Total organic carbon (TOC) and total inorganic carbon (TIC) were calculated after removing the carbonates by applying 10% HCl for 24 h, washing and then subtracting the remaining mass-weight from the total carbon.

The grain-size distribution of 0.5 cm^3 samples at discrete layers along the cores (*ca* 3 to 7 cm interval) was measured using a CILAS 1180 laser particle analyzer (CILAS Particle Size Analyzers, Orleans, France at the University of Geneva, Switzerland). For this purpose, samples were wet sieved below 1 mm and pretreated with 30% H_2O_2 to eliminate organic matter. Ultrasound in water bath was applied to the samples until the moment of measurement. Measurement of each sample was repeated twice or three times to validate the results. Grain size data was analyzed using the GRADISTAT software to obtain textural parameters and the textural classification of the analyzed sediments (Blott & Pye, 2001).

Microfacies analyses of laminated sediments

In order to focus this study on the lamination microstratigraphy, further analytical determinations were performed on sediments from the LSG2 core at higher-spatial resolution. Undisturbed sections were retrieved from the core using acrylic boxes (5 cm x 3 cm x 1 cm), freeze-dried and

then impregnated with degassed epoxy resin (araldite and hardener) under vacuum (University of Fribourg, Switzerland). From the impregnated blocks, 3 cm polished sections were prepared (University of Geneva, Switzerland), and then analyzed in a petrographic microscope under plain and polarized light. High resolution images were obtained with a digital camera.

Micro-elemental composition of the polished sections was inspected in 1.5 cm x 1 cm areas of interest, using an EAGLE III micro-XRF spectrometer (EDAX Inc., Mahwah, NJ, US) at the University of Geneva. Settlements included a Rh-tube, with 40 kV voltage, 375 to 675 μA current, dwell times of 4 to 10 ms per spot and overlapping 50 μm size in 25.6 μm steps. Multi-elemental maps (*ca* 1.5 cm length) were produced using overlies in the EAGLE evaluation software. The 15 cm thick section containing the volcanic ash from the terrace scarp (i.e. from outcrop 3) was also analyzed with the Eagle III micro-XRF spectrometer. In this case, a line measurement was performed using the same spectrometer settlements, changing the resolution to 0.5 mm.

Polished sections were subsequently analyzed by automated scanning electron microscopy using the FEI QEMSCAN® Quanta 650F (FEI Company, Hillsboro, OR, USA). This instrument provides maps of bulk mineralogy, texture, and chemical composition of different type of rocks and sediments without losing the particle structure or destroying the material. Mineral identification in this device is based on the combination of back-scattered electron, energy-dispersive X-ray spectra and X-ray count rates (Gottlieb *et al.*, 2000). Since the current study involved fine-grained sediments, the most valuable product was the mineralogical composition, and the mineral size, distribution and arrangement within each lamina. Measurements were performed at 15 kV, with a beam current calibrated at 10 nA.

Complementary microscopic images of the microfacies were obtained through smear slides preparation and analysis following the procedures of the LacCore Facility (http://lrc.geo.umn.edu/laccore/assets/pdf/sops/smearslides.pdf).

RESULTS

Outcrop and core stratigraphy

The gullies near the delta and a terrace scarp around LSG allowed the characterization of the stratigraphy above the present-day lake shoreline (**Figs 2 and 3A**), and their tentative correlation with the cores drilled from the lake shore (LSG2) and the lake center (LSG1) (**Fig. 3B**), which is based on the lithology and the stratigraphic position of beds.

Outcrops 1 and 2 in the main gully exhibit dark brown/dark grey-olive lacustrine muds at their base with presence of algal (macrophyte) remains, overlayed by a laterally continuous 5 to 10 cm thick white volcanic ash, which can be followed downstream and into the lake margin. Although the study of the ash is only complementary to the current study purpose, its presence sustains stratigraphic correlations since it can be used as a marker layer (**Fig. 3**). The top of outcrops 1 and 2 is formed by matrix-supported (reddish) and oriented clast-supported (grey) conglomerates (**Fig. 3A to C**). This likely represents a contraction succession, where lacustrine strata are truncated by fluvial-alluvial deposits. The lake terrace scarp (outcrop 3) exposes a lacustrine stratigraphy, including 72 cm thick faintly to well laminated dark greenish grey, brown and white sediments at the base, followed by 7 cm of the white ash deposit, and 34 cm of light greenish-grey, massive to faintly laminated mottled muds at the top of the sequence (**Fig. 3D**).

LSG2 core site is set next to the terrace scarp, *ca* 2 m above the present-day shoreline and *ca* 30 cm below outcrop 3 (**Figs 2** and **3**). Sediments are composed of 19 cm of dark laminated silts and clays, overlayed by 93 cm of white-grey-ochre-brown thinly laminated pack (**Fig. 4**). Then, the succession changes transitionally into 35 cm of grey to ochre sediments, with less evident laminated structures. Located at the centre of the lake (at 1 m water depth), in a lower topographic level than LSG2, the LSG1 core comprises 122 cm of massive greenish-grey sediments, overlayed in sharp contact by 28 cm of dark brown faintly laminated lacustrine sediments at the top of the sequence.

Based on the outcrop stratigraphy and the topographic profile (**Fig. 3**), the white volcanic ash appears younger than LSG2 core and it likely corresponds to the impenetrable level at the lake center (at the LSG1 bottom) that blocked the coring system. Microscopical observations at the basal layers of LSG1 show the presence of volcanic glass, which could be related to the underlying white ash. Therefore, this study considers that, despite the apparent inverted topography, LSG2 is stratigraphically older than LSG1 core.

Overall, the outcropping sections and the cores show a succession consistent with a lake contraction, after which the present lake dynamics has entrenched into its own previous expanded record.

Chronology

The chronology of the LSG record is constrained by seven radiocarbon ages (**Table 1**). The beginning of the record in this study (145 cm depth, LSG2 core) is older than 47,300 ^{14}C years BP,

beyond the radiocarbon calibration age limits. The sample from macrophyte remains collected from outcrop 1 at the gully (**Fig. 3**) also has an infinite radiocarbon age (**Table 1**). The uppermost sample (collected at 2 cm depth in LSG1 core) consists of macrofossils and ostracod shells and corresponds to modern ages (<1956 Common Era, CE) according to the AMS calibrated data. Preliminary radioisotope determinations of artificial ^{137}Cs indicate that fallout peak of 1964 CE recognized the Southern Hemisphere (**Appendix S1**) locates around the 10 to 12 cm level in LSG1 core. In addition, while the presence of unsupported ^{210}Pb is limited to the uppermost 20 cm of the LSG1 core, it is absent from LSG2 sediments (**Appendix S1)**. An absence of radiocarbon reservoir effect on the topmost part of the sequence is thus pointed by radiocarbon, ^{137}Cs and ^{210}Pb independent dating.

In general, ages follow a coherent stratigraphic order without reversals (**Fig. 4**). An exception exists in sediments from LSG2 core at the 123 cm level, where different dated materials show an offset of *ca* 15 ^{14}C kyr (**Table 1**). Potential sources of error could be attributed to a reservoir effect due to contamination with old carbon in the dated lacustrine organic matter at this depth (>45,500 ^{14}C yr BP; C/N = 6.52), which does not affect the larger ostracod shells (as observed in the modern age samples). Therefore, the younger 123 cm depth sample derived from carbonate shells, which also presents a lower error, is considered as more reliable and accepted for this study. Further discussion about the obtained ages is presented in the section titled *Considerations about the chronology*.

Radiocarbon dating (**Table 1**) and ^{210}Pb determinations (Appendix S1) confirm that the core LSG2 is older than the LSG1 core. The dates measured at the top of LSG2 (8 cm = 22.7 ± 0.1 ka) and the bottom of LSG1 cores (147 cm = 20.9 ± 0.1 ka) indicate that there is a gap of ~1.8 kyr between the LSG2 and LSG1 cores. The white volcanic ash marker layer is likely constrained within this gap (see section *Laguna La Salada Grande environment after ca 25.4 ka: shifts in the hydrological regime*).

Considering the nature of shallow-lake records in semi-arid environments, where periods of lake-bottom exposure and erosion are common and the presence of abrupt basal contacts observed along the LSG stratigraphy, data in this study only allows the estimation of minimum sedimentation rates. Assuming no hiatuses, the minimum linear sedimentation rate between 123 cm and 8 cm in LSG2 core would be 0.10 mm year^{-1}. For LSG1 core, the minimum linear sedimentation rate between 147 cm and 2 cm depth is 0.07 mm year^{-1}.

Sedimentary units

According to the described changes in colour, grain size, magnetic susceptibility and elemental composition, LSG1 and LSG2 composite sediment cores were classified into five sedimentary units (**Fig. 4A to C**). The record of LSG2 starts from unit E at the bottom and continues with units D and C (**Fig. 4A**). The LSG1 succession starts at the base with homogeneous unit B (divided into subunits B1 and B2) and finishes with unit A at the top (**Fig. 4C**). Chemical characteristics of the white ash layer are also represented between the LSG1 and LSG2 cores in **Fig. 4B**. The minimum age of the bottom and the top of every unit and subunit was estimated according to the sedimentation rate calculated on each core.

Unit E (149 to 130 cm; pre *ca* 34.8 ka; **Fig. 4C**) is composed of finely to thickly laminated dark brown and dark grey silts interlayered with light grey wavy laminae. These sediments are relatively TOC-rich and S-rich. In turn, Mn, K and Fe are relatively low. Calcium presents some sharp peaks, which follow the TIC trend, although element profiles are highly variable along the unit.

Unit D (130 to 35 cm; *ca* 34.8 to 25.4 ka; **Fig. 4A**) is formed by finely laminated muds composed of non-rhythmic alternations of white, ochre, grey and brown laminae. Most of the elements are highly variable. Total organic carbon and S values are low regarding the underlying sediments (unit E). Within unit D, a lamina composed of a dark-brown sandy ash was detected at 82 cm depth in LSG2 core.

Unit C (35 to 0 cm; *ca* 25.4 to ≤21.9 ka; **Fig. 4A**) is formed by grey muds with diatoms, sporadic ochre bands, and small (lateral extensions of <5 cm, thickness *ca* 1 cm) random sand lenses. This unit variates from diffused lamination to a homogeneous structure, contains finer particles than unit D, and presents less variable Ca, S, Fe, Mn and K counts. Total inorganic carbon percentages decrease upwards. The lower contact of this unit is transitional, and the upper contact is truncated by the ground surface.

At outcrop 3 (**Fig. 3)**, the 7 cm thick bed of consolidated white ash was deposited at an unidentified time after sediments correlated with unit C and before sediments correlated with unit B deposition (**Fig. 4B**). Its lower contact is abrupt with signs of oxidation marked by an orange-red band whereas its upper contact is transitional. Microscopic inspection shows a microcrystalline texture with *ca* 12% of crystals (plagioclase and pyroxenes were identified) in an amorphous and altered volcanic glass matrix (*ca* 88%). The XRF chemistry marks high Zr, K and Si counts.

Unit B (150 to 28 cm; *ca* 21.3 to 3.7 ka; **Fig. 4C**) comprises mainly massive green muds, with subtle variations along the stratigraphy that allow the division in two subunits. Subunit B2 (150 to 95 cm; *ca* 21.3 to 13.4 ka; **Fig. 4C**) is mostly composed of massive sticky green muds with a general uniform elemental composition. It shows sporadic ochre and dark-brown nodules marked by positive Mn excursions, and white aggregates accompanied by elevated Ca counts. Iron and K counts are high and do not show significant variations. Magnetic susceptibility presents high values at the base of the subunit, which could be related with the influence of underlying ash materials diluted at the base of subunit B2 sediments. This parameter then remains low for the rest of the subunit. Circular planktonic diatoms were observed through random microscopic observations along the subunit. Abundant volcanic glass fragments were identified at the base of the subunit.

Subunit B1 (95 to 28 cm; *ca* 13.4 to 3.7; **Fig. 4C**) is formed by massive green silts with white and red nodules, similar to subunit B2. It can be distinguished from subunit B2 by a lower thixotropic behaviour, an increase in magnetic susceptibility, Ca and Mn peaks, accompanied by variable Fe and K. Coarser particle sizes (silt and sand proportions) subtly increase compared to underlying subunit B2.

Unit A (28 to 0 cm; post *ca* 3.7 ka; **Fig. 4C**) is composed of banded to faintly laminated dark-yellowish-brown silts. At the base of the unit (between 26 cm and 22 cm), a sharp Ca peak, corresponding to a white dusty layer is present. The rest of the unit is characterized by relatively coarser, organic matter-rich and high Ca material interbedded with Fe-rich and K- rich layers. Along the unit, decoupled peaks of S and Mn are detected. The top of the unit contains ostracod valves reaching diameters >1 mm.

Multiproxy analysis

Along the profiles of the LSG2 and LSG1 cores (**Fig. 4**), remarkable variations and associations of petro-physical properties (MS, the mean grain size, and the range of medium silt to sand percentages), chemical composition (Fe, K, Ca, S and Mn counts, total organic and inorganic carbon) and elemental ratios (Zr/Fe, Inc/Coh) were detected. These parameters are regularly used as environmental proxies in palaeolimnological studies (Davies *et al.*, 2015).

Taken at face value, the parameters of LSG cores (**Fig. 4**) show a group of chemically stable elements (K, Fe and Zr), which have similar behaviour along the record. These elements are

commonly associated with detrital allochthonous minerals transported into lakes from their catchment area (e.g. Vogel *et al.,* 2010; Boës *et al.*, 2011; Kylander *et al.*, 2011). The Zr/Fe ratio has typically been associated with catchment erosion, transport of Zr-bearing minerals and flooding processes, where Zr concentrates in the heavier mineral silty or coarser grain-size fractions (e.g. Vogel *et al.*, 2010), while Fe concentrates in the clay fraction (e.g. Cuven *et al.*, 2010; Kylander *et al.*, 2011; Wilhelm *et al.*, 2013). In the LSG record, this ratio co-variates with the mean particle size, and especially with the coarsest sediment fraction (from medium silts to fine sands) (**Fig. 4**). Magnetic susceptibility values are variable but largely follow the grain size trend (**Fig. 4**).

Changes in oxygenation of the water column or at/below the sediment–water interface due to contrasting mixing regimes, biological productivity and sedimentation rates can be tracked by redox-sensitive metals such as Mn and Fe (Davison, 1993; Wetzel, 2001; Melles *et al.*, 2012; Francus *et al.*, 2013; Naeher *et al.*, 2013; Neugebauer *et al.*, 2018). In LSG cores, Mn and Fe curves are not coupled throughout the profiles and thus, both elements are not responding equally to oxygenation. In LSG, Fe variability seems to variate primarily due to changes in detrital input based on its close correspondence with redox-insensitive detrital indicators such as K. The Mn profile, on the other hand, displays an irregular behaviour in different units, but it generally shows positive Mn peaks in unit D, while it seems linked to some prominent Ca peaks in LSG1 core (**Fig. 4A** and **C**). Sulphur variations is as well related to oxygenation of the lake-bottom (Davies *et al.*, 2015). This element presents a complex behaviour along the LSG cores, with elevated counts in the dark organic matter-rich sections (units E and A).

The incoherent (Compton) / coherent (Rayleigh) scatter ratio (Inc/Coh) obtained from XRF scans, is an indicator for the average atomic number of a material (Davies *et al.*, 2015). Since organic matter and water are composed of elements with lower atomic masses than mineral phases, the ratio has commonly been used as an indirect proxy of organic matter (Burnett *et al*., 2011; Liu *et al*., 2013). In LSG cores, Inc/Coh ratios increase in the darker layers of both cores and are especially high in superficial sediments of unit A. On the other hand, calcium counts are also higher along most of LSG2 core, remain low and uniform along most part of greenish-grey muds from unit B (LSG1 core), and increase towards the dark-brown surface sediments (unit A).

Principal component analysis of proxies in the sedimentary units

The main chemical differences on each unit can be further visualized through PCA results. For the entire dataset (including LSG1 and LSG2 cores), two principal components explain about 70% of the total variance of elements and elemental ratios (**Fig. 5A**). PC1 explains 47.6% of the variance, and splits samples mostly associated to detrital lithogenic elements in the fine sediment fraction (Fe, K, Ti, Zn, Rb, Zr, Al, Ba, Si) versus biogenic (or endogenic) and coarse fraction elements and ratios (Ca, Ca/Ti, Sr, Si/Ti, Zr/Fe, Mn/Fe). Si/Ti ratio also suggests an association with this biogenic input, and it is probably related to biogenic silica from diatom frustules (Peinerud, 2000), which were microscopically observed along the entire record. On the other hand, Mn/Fe ratios are opposite to oxygenation due to differences in both elements' sensitivity to reductive dissolution with Mn being readily dissolved under reducing conditions while Fe is more likely to remain unaffected or to form stable authigenic phases. PC2 explains 22.3% of the variance and is anticorrelated with S, Cl, and positively correlated with Inc/Coh, Mn and Si, showing less clear geochemical pattern.

Sedimentary units are distributed in the biplot from **Fig. 5A** according to the interrelations of different elements and element ratios in every sample. While samples from unit D are mostly distributed along the coarse grained biogenic to fine-grained lithogenic element gradient, the rest of the units shows an influence of PC2 associated elements. Unit C samples are associated with the fine lithogenic fraction and slightly opposed to S and Cl. Subunits B1 and B2 are instead arranged around lithogenic elements of fine grains and Cl field, and unit A is linked to the biogenic fraction, S and Cl. The arrangement of samples in the biplot (**Fig. 5A**) and the peaks of element profiles (**Fig. 4**) point that S (opposed to Mn) is associated with the darkest sediments in units A and E. Therefore, it seems likely that PC2 is associated with reduced environments.

Changes in the chemical composition of sediments evidence significant variations of the lake conditions at the oldest part of the sequence. Thus, **Fig. 5B and C** present separate PCA biplots for the laminated units E and D. A similar pattern of sample distribution tied to fine lithogenic elements versus coarse and biogenic sediments is shown for both units, accounting for most of the variability (52% and 55%, respectively), distributing samples along this axis within both units. However, it is important to remark a change in the role of S played in the individual PCA of units E and D. Sulphur is only explained by PC2 axis in unit E and it is tied to its negative end in the Inc/Coh region (**Fig. 5C**). This is not the case for unit D (**Fig. 5B**), where S is linked to PC1 and the carbonate biogenic fraction. This shifting in S behaviour marks a change in the lacustrine status, which will be analyzed with more detail in the discussion.

Microfacies insights of laminated sediments from units E and D

Micromorphology of polished sections, smear slide inspection and automated analyses allowed insights into the different millimetric to sub-millimetric laminated structures as well as texture, and composition of each laminae distributed along units D and E. Based on these micro-analyses five different microfacies were identified: MF1 (*dark grey, organic matter-rich silt*s); MF2 (*brown bioclastic carbonate oozes*); MF3 (*ochre clayey muds*); MF4 (*dark grey sandy silts*); MF5 (*white carbonate muds*), which main characteristics and arrangement, as well as the interpretation of their depositional environment are summarized in **Table 2** and illustrated in **Figs 6** and **7**.

The general distribution of these microfacies along LSG2 core shows MF1 and MF2 usually forming couplets of laminae in unit E, while in unit D (**Fig. 6A**), the general intercalation pattern of laminae (MF2, MF4/MF1, MF3, MF5, **Fig. 6B to L**) becomes more variable.

Overall, the sections of units E and D show that the major mineral composition includes illite $(K,H3O)(Al,Mg,Fe)_2(Si, Al)_4O_{10}[(OH)_2,(H_2O)]$, quartz ($SiO_2$), plagioclase ($NaAlSi_3O_8$ – $CaAl_2Si_2O_8$) and calcite/aragonite ($CaCO_3$) (**Fig. 7**). Minor and trace minerals include biotite, montmorillonite, K-feldspar, pyrite, muscovite, gypsum, enstatite, apatite, kaolinite, chlorite, glauconite and hornblende. Variable isotropic volcanic glass fragments are detected in the sections (**Fig. 6**).

The most remarkable feature of laminated microfacies in the micro-XRF results is depicted by the distribution of Ca and Fe counts forming the laminae, which exhibit a specular pattern at centimetric and millimetric scales (**Fig. 7A to H**), also evidenced statistically by PC1 extremes (coarse bioclastic versus fine lithogenic) in both units (**Fig. 5**). These laminae are thicker in unit E than in unit D. QEMSCAN data show that the Fe-rich laminae are mainly associated with fine-grained illite, whereas the Ca-rich laminae are mainly composed of large aragonite/calcite bioclasts (sometimes parallelly oriented to lamination), including some quartz and plagioclase grains with a variable matrix content (**Fig. 7D to F**). In turn, S counts increase towards the center of unit E (*ca* 135 to 132 cm), not matching neither with Ca nor with Fe patterns (**Fig. 7A**), and show uniform and extremely low counts along the overlaying unit D. A closer inspection of the QEMSCAN results in unit E shows that minor amounts of pyrite are in framboidal form and infilling the inside walls of bioclasts (**Fig. 7F**) or associated with organic matter aggregates and diatom valves **(Fig. 6F)**. Silicon is observed overall the sections of both units, although some larger Si-rich particles are concentrated intra-laminae in discrete irregular laminae (**Fig. 7G**). As

previously shown, high Si/Ti ratios (**Fig. 4**) indicate a possible contribution of biogenic silica (diatoms), which is revealed by the thin sections along both units (**Fig. 7C**). Manganese is dispersed inside the laminae or accumulated at the contact of the Ca-rich laminae and the base of Fe-rich consecutive laminae of unit D (**Fig. 7G**). In contrast, prominent Mn peaks are not found in unit E.

DISCUSSION

Due to its small size and limited drainage area located in a high-relief region, the currently shallow-lake system of LSG can be easily overlooked as a long-term palaeoenvironmental record. However, its small drainage area with limited allochthonous provenance, as a product of the topographic restriction to sediment input, combined with the arid climate (Cohen *et al.*, 2014), makes this lake record suitable to preserve Quaternary primary sedimentation features. The presence of outcropped sections allows a correlation of the exposed deposits with the underwater sediments (cores), which complement and reinforce the interpretations of the past lake system environments. Since the lake watershed was not affected by recent glacial activity, the record extends beyond the LGM period, in a time-range with reduced lacustrine records in high-mountain areas, like the central Andes. Moreover, its water level response, largely linked to the main moisture front from the monsoon system, turns LSG deposit as a high-fidelity candidate record for tracking regional climate signatures.

Considering the peculiar attributes of LSG, the discussion of the results is divided into four sections. The first section evaluates the strengths, limitations and potential errors of the obtained chronology. The second section examines in detail the processes occurred in the lake and its catchment that led to the formation and preservation of the thinly laminated sediments, which correspond to the period prior to 25.4 ka (units E and D). The third part of the discussion debates the shifts occurred in LSG after 25.4 ka to the present (units C, B and A), which are mainly interpreted from homogeneous finer sediments. An additional consideration of the correlation and regional value of the white volcanic ash is included within this section. Finally, the last section is focused on the climate significance of the LSG sedimentological record. It summarizes the palaeoenvironmental changes occurred in the lake system and inserts the reconstruction into a broader context during known global climatic stages occurred since the MIS 3 to the present. The multifocal study of this lacustrine sequence provides valuable and detailed information of

depositional dynamics in small closed lakes at mountain foreland basins during contrasting climate situations.

Considerations about the chronology

The reliability of the chronological model is critical for inserting the local palaeoenvironmental data in the regional or global palaeoclimate context. Beyond this study's results, radiocarbon dating in lacustrine records from the arid and semi-arid mountains of the Central Andes is usually considered a challenge due to: (i) the general scarcity of terrestrial organic matter accumulated in sediments suitable for dating; and (ii) a common and variable reservoir effect and old carbon incorporation from different sources affecting the age of non-terrestrial carbon fractions of the deposits. This problem has been mentioned and discussed in most of the literature from the area (e.g. Geyh *et al.* 1998, 1999; Sylvestre *et al.,* 1999; Valero Garcés *et al.,* 1999; Grosjean *et al.* 2001, Placzek *et al*., 2006; McGlue *et al.,* 2013; López Steinmetz & Galli, 2015; Pfeiffer *et al.*, 2018 and references therein). In addition, gaps induced by subaerial exposure and erosion of lake deposits (McGlue *et al.*, 2017) are frequent and not always detectable in the records from arid mountain landscapes, affecting the consistency of chronological models. In particular, the obtained LSG chronology presents strengths and uncertainties regarding the age model reliability.

Results from this study supply confident evidence about the stratigraphic order of the LSG composite cores, where individual ages are mostly coherent among each other and consistent with the correlation between cores and outcrops presented in the section titled *Outcrop and core stratigraphy*. For instance, the presence of abundant volcanic glass at the base of the LSG1 core suggested that the white volcanic ash layer observed in outcrops above the LSG2 core underlays the base of the LSG1 core underwater, showing a topographic inversion of both cores. Evidence supplied by independent dating methodology (^{210}Pb, ^{137}Cs, see Appendix S1; AMS, see **Table 1**), demonstrates that the LSG1 core contains the most recent part of the record (i.e. 150 years), in unit A, and that LSG2 sediments are significantly older, supporting the interpretation based on fieldwork observations.

Unlike other works from the central Andes (e.g. Grosjean *et al*., 2001), the uppermost dated sample from unit A (at 2 cm depth) did not present a ^{14}C reservoir effect. Although it is not considered for the purposes of this work, a minor offset between the calibrated radiocarbon age

marking 1957 CE at 2 cm depth, and the ^{137}Cs profile, which marks the peak of 1963 CE around 10 cm depth was observed.

At level LSG2-123 cm, the age difference between paired samples detected on the bulk sediments and the meshed organic matter fraction with ostracods (Table 1), implies an error in one of both results. A radiocarbon reservoir effect would explain too old ages in bulk organic matter and can be produced by waters depleted in ^{14}C. In this case, the younger results from ostracod shells obtained in LSG would be the real age. Geyh *et al*. (1999) linked reservoir changes to important lake level variations in a lake from Atacama, Central Andes, causing periods of equilibrium/disequilibrium of dissolved carbon in water with atmospheric CO_2. The palaeoshorelines around the current lake in LSG, located several metres above the present-day lake level, point to similar triggers for LSG reservoirs. An incorporation of old material from the catchment would also lead to strong age offsets in bulk samples. Alternatively, contamination with younger carbon resulting in younger apparent ages were interpreted by Placzek *et al.* (2006) in the same region. If this was the scenario in LSG, the younger age from sample at 123 cm should be considered as a minimum age, and the real age would remain unknown. Taking into account both arguments, this study considers the youngest age at LSG2-123 cm depth with lower error, as the most probable real age for this work.

In contrast to sample at LSG2-123 cm depth, very low organic matter amount found in the sample from unit B at LSG1-147 cm depth prevented cross-checking data by dating different carbon fractions. Therefore, the age obtained from bulk samples in unit B might be considered with caution because it could represent a maximum age. Next works in LSG record should explore alternative chronologies independent from radiocarbon to constrain the age results provided in this work. With the considerations mentioned in the above discussion, the depositional processes occurred in LSG can be analyzed with different levels of detail and synthesized in a palaeoenvironmental reconstruction contrastable with well-recognized palaeoclimate stages.

Laguna La Salada Grande environment pre-25.4 ka: laminae formation processes

The LSG2 record accumulated prior to 25.4 ka comprise laminated units E and D. Through the observation of the microfacies (microchemical composition, texture and internal structures), as well as their interrelation and distribution, it is possible to discuss the main processes leading to

the formation (and preservation) of laminae, including lake level variations, changes in oxygenation conditions and, mainly, the influx of relatively coarse sediment.

Non-regular laminae of unit E are composed of fine-grained Fe-rich muds (MF1), forming the background pelagic sedimentation, interrupted by mixed bioclastic and detrital silts (MF2; **Figs 6** and **7**; **Table 2**), showing alternation of periods of high organic matter (OM) productivity and settling down of fine-grained sediments with punctuated higher-energy clastic input. The preservation of lamination containing organic matter-rich sediments is usually enhanced by the following conditions: (i) relatively deep-water column with minimal disturbance of the lake bottom (for example, by reworking); (ii) lake bottom anoxia (for example, due to periods of thermal or chemical stratification); (iii) accumulation of OM exceeding the siliciclastic or/and carbonate sedimentation and the OM-decay by microbial activity (Glenn and Kelts, 1991; Kemp, 1996; Last, 2002; Renaut & Gierlowski-Kordesch, 2010). The present-day location of LSG2 core, 15 m away from the shoreline in an emerged supralittoral environment (**Figs 2A**, 2**B and 3**), unequivocally demonstrates that during deposition of units E and D the lake had a larger extension and a higher-level than at present. Lacustrine OM-rich dark sediments found upstream in the sections along the main gully (**Fig. 3B** and **C; Table 1**) can be correlated to the oldest unit E, likely indicating that the lake was more extended than present and revealing that deposition occurred in a relatively profundal and calm lake environment. An elevated palaeodelta and palaeoshorelines preserved around the lake (**Fig. 1B**) support the interpretation of higher lake levels in the past. Additionally, the formation of surface ice in some sectors of LSG was observed during fieldwork, which implies that this supplementary process could be enhanced during cold glacial times in the region (Zech *et al*., 2009; Martini *et al*., 2017a), contributing to periods of lake water stratification.

The transition between units E and D (*ca* 34.3 ka; **Fig. 4C**) is characterized by the shift of OM and S behaviour pointing to a change in the lake system. Data obtained from the microanalysis, statistics and mineralogical maps in unit E indicate low-oxygen conditions caused by the deposition of thick OM-rich laminae with the formation of pyrite (**Figs 4, 5C** and **6**). In contrast, in overlying units (D, C and B), OM and S concentrations are extremely low (**Figs 4** and **7**), revealing that relative anoxia ceased. Furthermore, microfacies characterization in unit D shows occasional cracks and deformation structures in the fine ochre muds (MF3; **Fig. 6F**) caused by rapid heavier sandy silts loads from MF4, and Mn accumulations at some laminae (MF2/MF1) boundaries (**Figs 4A** and **6A**). This suggests periods with variable water levels, high oxygenation

and events of high-energy supply, which are typical processes in littoral-sublittoral environments in shallow lakes (Carrol & Bohacs, 1999), pointing to a general lake level drop during deposition of unit D (**Fig. 8**). Therefore, the transition from unit E to D indicates a lake contraction, although under general deeper conditions than at present day (i.e., considering the LSG2 site position above the present lake-level; **Fig. 3**).

Another important discussion subject arises from the transport processes leading the coarse-grained deposition. The irregular intercalation of coarse MF2 and MF4, which present abrupt irregular-basal contacts, within the fine-grained sediments from MF1 and MF3, forming non-rhythmic laminae along units E and D, reflects unevenly spaced events of high-energy discharges probably associated with sporadic floods. MF4, mainly developed in unit D, shows signs of transport evidenced by clast-supported siliciclastic and heavier minerals, which would suggest watershed erosion and carriage of exogenic materials into the lake, and could be possibly associated with former deltaic activity. Parallel orientation fabrics of fragmented ostracod valves occasionally observed in MF2 together with variable terrigenous material may indicate transport of bioclasts from littoral areas and allogenic grains to the depozone. A closer look into MF2 shows the presence of charophyte remains (**Table 2**). Charophytes are macroscopic green algae commonly occurring in the littoral zone of lakes forming dense communities, and their presence indicates photic conditions (Pełechaty *et al*., 2013; McGlue *et al*., 2017). Their growth is limited by light, salinity, nutrients and temperature under shallow water. As charophyte fragments (calcified charophyte thalli and gyrogonites) were found dispersed in some layers with coarse-grained minerals, their deposition was considered the result of intra-lacustrine high-energy transport from littoral environments.

Taking into account the (minimum) linear sedimentation rate calculated for LSG2 core an initial inspection of the frequency of high-energy events can be assessed by evaluating the XRF counts of Zr/Fe ratio and Ca positive peaks (**Fig. 4C**). Since high Zr/Fe ratios largely represent the deposition of siliciclastic medium silts to sands (**Fig. 4**), they can be used to recognize periods of increased transport of exogenic material into the lake (e.g. Cuven *et al.*, 2010; Wilhelm *et al.*, 2013). A number of 62 positive peaks were visually counted in unit E (21 cm total thickness, unknown age range) and 249 in unit D (93 cm total thickness representing 9.38 kyr). Likewise, Ca positive peaks mainly represent the bioclastic material from MF2, which are interpreted as re-transported by high-energy events. A total of 50 Ca and 206 Ca peaks were counted in units E and D, respectively. Considering these counts, a first approximation average of one high-energy influx

event occurring every *ca* 37 to 45 years can be estimated for unit D. Unfortunately, the uncertainty about the basal age of unit E (see **Table 1**, infinite radiocarbon age) only allow estimation that a lower frequency of events occurred along this unit. A reduced frequency is also compatible with a deeper lake and deposition in intermediate to profundal lake zones. Moreover, the amplitude of the peaks and their distribution along the units are not uniform, indicating that their periodicity and intensity variated along time. Irregular runoff records are characteristics of arid and semi-arid environments, where floods are variable and erratic events, largely dependent on the storm intensity and duration (Alexandrov *et al.*, 2009). In this kind of setting, extended dry periods without intense-flooding events are common (Alexandrov *et al.*, 2009), promoting low-energy sedimentation in lakes, while large new high-energy depositional episodes can erase the older ones, which can explain the non-rhythmicity or dyscyclicity (*c.f.* Einsele, 2000) of preserved depositional events in LSG. This is evident for unit D sediments where fine silt and clay layers are partially truncated by the MF4. At present day, episodes of extreme runoff and mass movement in the semi-arid Cordillera Oriental are usually produced by intense summer convective storms (Castino *et al.,* 2016, 2020), linking the local response of LSG coarse-detrital flux dynamics and lake infill to large-scale fluctuations of monsoonal climate features. Thus, the LSG lamination marked by coarse lithogenic Zr/Fe and Ca peaks occurred before 25.4 ka can be considered as the record of flooding events triggered by convective storms linked to SASM past activity, surpassing the littoral environments and producing hyperpycnal flows.

Laguna La Salada Grande environment after *ca* 25.4 ka: shifts in the hydrological regime

Overlaying unit D, faintly laminated to massive muds from unit C (starting at *ca* 25.4 ka) are marking a transitional period, with limited lamination and reduced detrital and carbonate input (**Fig. 4**). According to this study's correlation, the white volcanic ash layer is deposited after or within unit C. Nevertheless, the provenance and regional extension of this tephra is unknown. During the Late Quaternary, records of explosive activity extend through the Andean Central Volcanic Zone (16° to 28°S) (Schellenberger, 2008; Placzek *et al*., 2009). The white volcanic ash presented in this work, which can be tracked around the entire basin with a considerable thickness (5 to 15 cm), could be studied as a chronostratigraphic marker for the Late Pleistocene in the region. The obtained radiocarbon dates bracketing the temporal range of this tephra (22.7 to 20.9 ka) could help future works for correlation and synchronization of sediment records with similar ages. Considering the geographic localization of the white volcanic ash at LSG, its rhyolithic

composition and the age, the most probable source of this deposit corresponds to the Cerro Blanco Volcanic Complex (Baez *et al*., 2015) at the southern Puna region. Due to its location, the ash would be transported by westerly winds. Nevertheless, further geochemical analyses and independent dating of this tephra are needed to establish the source and dispersion area of the ash, and the exact timing of the eruption.

After a gap in this study's record of unknown extension, where the white ash is contained (**Fig. 4**), the sequence continues with units B (starting at 21.3 ka) and A from the LSG1 core. Despite the homogeneity of unit B diminishes the extent of the interpretation of environmental variations at short timescales, it marks a significant change in LSG regime. Sedimentation rates for units B are lower than the older units suggesting either erosion (although not evident in the record), or low accumulation rates due to a reduced extent or lower efficiency of the transport agent (i.e. limited runoff). In the LSG environment, the latter option (i.e. low accumulation) would imply a weakened impact of convective storms triggering the movement of terrigenous material to the depocenter, contrasting with the previous units D and E. Moreover, fine-grained sediments (especially in subunit B2) and the absence of bioclastic fragments in unit B (**Fig. 4A**), indicate that the former mechanism supplying coarser exogenic and littoral material to units E and D decreased its capacity, receded or deactivated. This could be explained by a change of watershed configuration produced by, for example, the deactivation of the former palaeodeltas due to lake expansion and a consequent broader separation between the proximal littoral belt and the profundal area (**Fig. 2**). Even when homogeneity of unit B sediments could indicate lake bottom disturbance, the presence of correlated lacustrine sediments overlying the white volcanic ash at proximal parts of the gully, several metres away from the present-day shoreline (**Figs 2B and 3**), implies that the lake was larger than at present, at least during fine-grained part of subunit B2 deposition.

Overlying unit B, dark unit A marks an important change to high OM accumulation and positive sulphur peaks. The sedimentation rate calculated for LSG1 core situates unit B-A contact at 3.7 ka, although preliminary ^{137}Cs and ^{210}Pb dating indicates that the last 20 cm sediments are younger than 100 to 150 years, increasing sedimentation rates in unit A (Appendix S1). Considering the basin stratigraphy and the surrounding geomorphology, an abrupt lake-level drop is suggested for a still unknown time between subunit B1 and unit A, generating the exposure of a large part of the lake bottom and the formation of gullies due to fluvial incision on LSG sediments

(**Fig. 2**). This dry period could coincide with an abrupt positive Ca peak at the base of unit A, concomitant with low lithogenic element counts at the XRF profile (**Fig. 4C**).

Laguna La Salada Grande record in the palaeoclimate context

The LSG units contain evidence of changes in the depositional processes and lake-level fluctuations since the Late Pleistocene that can be compared with different contemporary palaeoclimate archives in subtropical South America, generally evidencing well-matched moisture signals over multi-millennial scale (**Fig. 8A to F**). These long-lasting changes in precipitation have been attributed to summer insolation variations over subtropical South America, which modulates the position of the ITCZ and its component parts controlling the intensity of the SASM (Baker *et al.*, 2001; Cruz *et al.*, 2006; Placzek *et al.*, 2006; Wang *et al.*, 2007; Cheng *et al.*, 2012; Baker & Fritz, 2015).

During the Late Pleistocene, global climate shifted from the Last Interglacial (*ca* 130–116 kyr BP) to the full glacial state of the LGM (26.5 to 19 ka; Clark *et al.*, 2009), including intermediate interstadial and stadial stages. Palaeoenvironmental records in high-mountain areas, as the central Andes, for the period prior to the LGM are largely restricted mostly because of low preservation of well-dated archives in glaciated areas (Gasparini *et al.*, 2016; Stojakowits *et al.*, 2021). According to the study's age model and palaeoenvironmental reconstruction, the sedimentary units E and D represent stages of contrasting lake conditions in a time period preceding the global LGM. Starting with the oldest OM-rich and S-rich laminated unit E, a relatively deep, and often stratified palaeolake stage can be assumed for the period prior to *ca* 34 ka (**Fig. 8D to F**). This stage can be tracked until the bottom of core LSG2 (the base of the unit was not reached), which is marked by an infinite radiocarbon age (**Table 1**). This unit correlates in time with the part of MIS 3 interstadial occurred from 57 to 29 ka (**Fig. 8**) and can be tracked as a humid period along the region. Wet phases contemporary to unit E were interpreted from Brazilian speleothems in the Botuverá cave (27°S) (Wang *et al.*, 2007; **Fig. 8A**) and well-documented lacustrine records from the Bolivian Altiplano, such as the Inca Huasi (*ca* 46 ka; Placzek *et al.*, 2006) and Minchin (*ca* 46–36 ka; Baker *et al.*, 2001; Fritz *et al.*, 2004; Nunnery *et al.*, 2019; **Fig. 8B**) highstand palaeolakes. Archives located closer to LSG, partially concomitant with unit E, register glacial advances at Nevado de Chañi in the high mountains of Cordillera Oriental (between 52 ka and 39 ka, Martini *et al.*, 2017a, **Fig. 8C**), lake expansions at Laguna Pozuelos in

the Puna region (McGlue *et al.*, 2013, 2017) and terrace accretion in the western side of Humahuaca valley (Schildgen *et al.*, 2016).

From 34 to 25 ka, a change from deeper and stable to shallower lake conditions is recorded in unit D, deposited during the last part of MIS 3 towards MIS2 transition (**Fig. 8D to F**). It is important to remark that over this shallower-lake stage, frequent high-energy clastic discharges, probably related to heavy sub-centennial rainfall events, were identified and measured through LSG sediment lamination (as discussed in the section *Laguna La Salada Grande environment after ca 25.4 ka: shifts in the hydrological regime*). The dynamic deposition and unstable environmental conditions were likely induced by frequent events of strong convective activity at the eastern part of the Cordillera Oriental, interrupting relatively arid conditions during the last warmer part of MIS 3 (**Fig. 8**). Most of the analyzed sites, both local (McGlue *et al.*, 2013, 2017; Torres *et al.*, 2016) and regional (Fritz *et al.*, 2004; Wang *et al.*, 2007; Nunnery *et al.*, 2019; **Fig. 8**), show high effective moisture variability during this interval. Interestingly, there are no glacial records contemporary to unit D in the region (**Fig. 8C**) (Zech *et al.*, 2009; Martini *et al.*, 2017a; D'Arcy *et al.*, 2019), which is compatible with increased aridity inferred for the area and mild global temperatures. Unlike the millennial changes, precipitation variations of shorter-term modes (for example, El Niño Southern Oscillation-like oscillations) have been less investigated for Late Pleistocene archives from North-western Argentina due to the scarcity of high-resolution data in semiarid or arid environments. In this matter, LSG laminated sediments unveil high-frequency modes occurred during the Late Pleistocene in this region taking part during the interstadial-stadial transition.

The LSG record between *ca* 25 ka and *ca* 22 ka is represented by unit C, displaying similar but less variable conditions than unit D (**Fig. 8D to F**), with diminished carbonate accumulation. Even when unit C is contemporary with part of the Last Glacial Maximum (26.5 to 19 ka; Clark *et al.*, 2009), which is globally recognized, abrupt imprints of this period are not clearly distinguished within this unit. In contrast, the LGM is well-documented by an important glacial advance at the Nevado de Chañi massif (Martini *et al.*, 2017a; **Fig. 8C**) coinciding with a high precipitation phase in the speleothems from south-east Brazil (**Fig. 8A**; Wang *et al.*, 2007; Novello *et al.*, 2017). It is remarkable, though, that the lacustrine reconstructions during the LGM along the subtropical Andes show variable signals regarding the extent, magnitude and timing of lake-level phases during this interval (Baker *et al.*, 2001; Fritz *et al.*, 2004; Placzek *et al.*, 2006; Blard *et al.*, 2011; Baker & Fritz, 2015).

Starting at the end of the LGM (*ca* 21 ka), unit B exposes a critical shift in the lake regime marked by an increase of water depth, fine-grained sedimentation, and an associated change of the catchment configuration (**Fig. 8D** to **F**). Contemporary to subunit B2, two glacial expansions were recorded at the Nevado de Chañi massif (at *ca* 15 ka and *ca* 12 ka; **Fig. 8C**), mostly coinciding with Tauca (18 to 14 ka) and Coipasa (13 to 11 ka) (Placzek *et al.*, 2006; Blard *et al.*, 2011) palaeolake highstands in the Altiplano, and roughly with wet stages in the Atacama Desert (Quade *et al.*, 2008) and the Botuverá speleothems (Wang *et al.*, 2007; **Fig. 8A**). The record of Laguna Pozuelos indicates the development of an extended saline palaeolake (McGlue *et al.*, 2013, 2017). This comparison suggests a period with pulses of high precipitation over a wide area of the SAMS domain, which is rather recorded as a long interval of high-water levels without recognizing short-term fluctuations in homogeneous unit B.

Moving forward to the current interstadial (MIS 1), an abrupt lake-level drop was interpreted, with consequent the readjustment of base levels, producing the fluvial incision (gully) and terrace scarp formation over the LSG lake sediments (**Figs 2, 3** and **8**). The incision occurred at an undefined time between subunit B1 (~13 ka) and unit A (<3.7 ka, >100 to 150 years). In agreement, a general aridification was recognized in North-western Argentina from *ca* 9 ka and intensifying during the middle Holocene (Schabitz *et al.*, 2000; Tchlinguirian & Morales, 2013; López & Galli, 2015; Torres *et al.*, 2016). Particularly in the lacustrine record of Laguna Pozuelos, a hiatus was constrained between 13 ka and 7 ka (McGlue *et al.*, 2017). If the middle Holocene hiatus is present in LSG records, it is not evident in the homogeneous sediments of unit B. In turn, it could be presumed at the marked sedimentological change at base of unit A (**Fig. 4C**) but further dating would be required to test this hypothesis. In any case, the palaeoenvironmental reconstruction of LSG inserted into a broader palaeoclimate context highlights the prominent role of hydroclimate activity modulating the infill of mountain lakes at non-glaciated arid areas, where detrital deposition during times of increased effective moisture (either episodical interrupting relatively dry periods, or sustained during more humid stages) is balanced by erosion (during phases of extreme aridity), producing a delicate equilibrium that favors lake persistence and long-lasting palaeoenvironmental records.

Finally, unit A represents the youngest part of the LSG record, mostly characterized by organic-rich material and increased sedimentation rates (**Fig. 8D to F**), which can be attributed to anthropic activity during the last centuries as have been shown in other wetland archives in the

fragile high-altitude ecosystems of North-western Argentina (Schiteck *et al.*, 2016; Lupo *et al.*, 2018; Hooper *et al.*, 2020).

CONCLUSIONS

The lacustrine record from Laguna La Salada Grande (LSG) presents a succession of laminated to massive sediments extending back to the Late Pleistocene. Geochemical and petrophysical analyses allowed the identification of sediment influx, organic matter accumulation and oxygen conditions as the dominant factors controlling the chemistry, structure and texture of the LSG deposits. Stratigraphic and geomorphological features surrounding the lake supplied additional evidence of palaeoenvironmental changes that occurred within the lake and in its watershed. Additional information about a tephra marker layer recognized in the lake stratigraphy is provided for ongoing studies of Late Pleistocene eruptions in North-western Argentina and the potential influence through westerlies of the central Andean volcanic zone.

The LSG sediments document contrasting palaeoenvironmental stages in a high-mountain closed lake from, at least, *ca* 34 ka to the present. Millennial-scale environmental changes characterize most of the record and shorter-time depositional event signals are recognized in laminated units. The most contrasting wide stages include the development of: (i) a relatively deep stable palaeolake, with probable stratification and anoxic periods formed under a wetter climate before *ca* 34 ka; (ii) a shallower more unstable palaeolake during drier conditions until *ca* 25 ka represented by thinly laminated sediments; (iii) a relatively deeper to intermediate lake stage with an homogeneous record initiated at least at *ca* 21 ka; (iv) an abrupt lake level drop preceding the installation of; (v) the current shallow lake. The general agreement of LSG units with other palaeoclimate records in subtropical South America indicates that the adjustments of the lake likely followed multi-millennial changes of the past South American Summer Monsoon (SASM) dynamics superposed on a long-term contraction trend associated to increasing aridity during the Holocene.

Automated mineralogical-geochemical techniques, combined with detailed microfacies analysis over laminated lake sediments, were applied for the first time in North-western Argentina in order to understand the controls on laminae formation and proxies' behaviours within lamination. The micro-stratigraphy approach considering high-energy flood recurrence intervals of sedimentation in LSG laminated units sets the basis for future works of event stratigraphy and non-stationary time analysis in high-mountain semi-arid lacustrine environments, allowing the

identification of the discharge-event modes via facies and microfacies modeling. In this sense, LSG sediments constitute, an invaluable high-resolution palaeoenvironmental record of high-energy processes infilling closed lakes located on top wedge basins, under changing climate conditions, like during the transition from interstadial (MIS 3) to stadial (MIS 2). Particularly, this is a remarkably understudied time period in arid and semi-arid high mountain areas, including North-western Argentina, with significant implications for the reconstruction of global past climates.

ACKNOWLEDGEMENTS

Most of this research was possible thanks to the Swiss Confederation through Swiss Government Excellence Scholarships for Foreign Scholars 2017-2018 in the Department of Geological Sciences at the University of Geneva to the leading author. Field work and sediment shipment was founded with PICT-2013-1371/PIP-CONICET 112-201101-00759 and PICT 2016-0673. We particularly thank geologists Eliseo Flores (CICTERRA) and Francisco Muñoz (Universidad de Córdoba) for their intensive and invaluable collaboration in the fieldwork, Dr Lucía Domínguez at the University of Geneva for her support in grain size analyses, and Jean-Charles Schaegis at the University of Fribourg for his help in the sediment embedding preparation. The XRF measurements and radiocarbon dating were founded by the Limnogeology Group of the University of Geneva. We would also like to thank the Millennium Nucleus Paleoclimate (NCN17_079) and the Universidad de Chile. Part of the research was supported by ANID/CONICYT + FONDECYT Postdoctorado + Folio (3190861). Our most special thank is to Doña Ricarda Aparzo and Don Tomás Condorí by their warm welcome and hospitality during the fieldwork, and the local residents who live in Jujuy, close to the Laguna La Salada Grande for their hospitality. We also thank Dr Francisco Córdoba (Instituto de Ecorregiones Andinas, Universidad Nacional de Jujuy) for his hospitality and contributions with the discussion about the working site definition. We thank the anonymous reviewers for reading the manuscript and for their valuable comments that contributed to improve our work. We are very grateful to the Editorial Board of *Sedimentology*, Dr Peir K. Pufahl, Dr Lauren Birgenheier, Elaine Richardson and Christa Koebernick for their kind help during the submission process.

DATA AVAILABILITY STATEMENT

The data that support the findings of this study are available within the article, and from the corresponding author upon reasonable request. We declare that we do not have any conflict of interest in connection with this work.

REFERENCES

Alexandrov, Y., **Cohen, H.**, **Laronne, J.B.** and **Reid, I.** (2009) Suspended sediment load, bed load, and dissolved load yields from a semiarid drainage basin: A 15-year study. *Water Resour. Res.*, **45**, 1–13.

Alloway, B. V., **Lowe, D.J.**, **Barrell, D.J.A.**, **Newnham, R.M.**, **Almond, P.C.**, **Augustinus, P.C.**, **Bertler, N.A.N.**, **Carter, L.**, **Litchfield, N.J.**, **McGlone, M.S.**, **Shulmeister, J.**, **Vandergoes, M.J.**, **Williams, P.W.**, **Anderson, B.**, **Brackley, H.**, **Burge, P.**, **Carter, J.**, **Cochran, U.**, **Cooke, P.**, **Crampton, J.**, **Crouch, E.**, **Crundwell, M.**, **Deng, Y.**, **Drost, F.**, **Graham, I.**, **Harper, M.**, **Hayward, B.**, **Hendy, C.**, **Hollis, C.**, **Hughes, M.**, **Kennedy, D.**, **Kennedy, L.**, **King, D.**, **Mackintosh, A.**, **Manighetti, B.**, **Marra, M.**, **Mildenhall, D.**, **Morgenstern, U.**, **Naish, T.**, **Neil, H.**, **Nobes, D.**, **Page, M.**, **Palmer, A.**, **Prior, C.**, **Rieser, U.**, **Rother, H.**, **Shane, P.**, **Strong, P.**, **Suggate, P.**, **Thomson, J.**, **Tonkin, P.**, **Trustrum, N.**, **Van Dissen, R.**, **Vucetich, C.**, **Wilmshurst, J.**, **Woodward, C.** and **Zondervan, A.** (2007) Towards a climate event stratigraphy for New Zealand over the past 30 000 years (NZ-INTIMATE project). *J. Quat. Sci.*, **22**, 9–35.

Amao, A. O., Al-Ramadan, K., & Koeshidayatullah, A. (2016). Automated mineralogical methodology to study carbonate grain microstructure: an example from oncoids. *Environmental earth sciences*, **75**(8), 1-11.

Arche, A. (2008). Some precisions on the use of the term playa in the geologic literature. *Journal of Iberian Geology,* **34** (1), 5-9

Báez, W., Arnosio, M., Chiodi, A., Ortiz-Yañes, A., Viramonte, J.G., Bustos, E., Giordano, G. and **López, J.F.** (2015) Estratigrafía y evolución del Complejo Volcánico Cerro Blanco, Puna Austral, Argentina. *Revista Mexicana de Ciencias Geológicas*, **32**(1), 29-49.

Baker, P.A. and **Fritz, S.C.** (2015) Nature and causes of Quaternary climate variation of tropical South America. *Quat. Sci. Rev.*, **124**, 31–47.

Baker, P.A., **Rigsby, C.A.**, **Seltzer, G.O.**, **Fritz, S.C.**, **Lowenstein, T.K.**, **Bacher, N.P.** and **Veliz, C.** (2001) Tropical climate changes at millennial and orbital timescales on the Bolivian Altiplano. *Nature*, **409**, 698–701.

Ben Dor, Y., **Neugebauer, I.**, **Enzel, Y.**, **Schwab, M.J.**, **Tjallingii, R.**, **Erel, Y.** and **Brauer, A.** (2019) Varves of the Dead Sea sedimentary record. *Quat. Sci. Rev.*, **215**, 173–184.

Bianchi, A. and **Cravero, S.** (2010) Atlas climático digital de la República Argentina. *INTA*, 55 pp.

Bianchi, A. and **Yañez** (1992) Las precipitaciones del Noroeste Argentino: Salta.*Instituto Nacional de Tecnología Agropecuaria Estación Experimental Agropecuaria*, Salta, 393 pp.

Blard, P.H., **Sylvestre, F.**, **Tripati, A.K.**, **Claude, C.**, **Causse, C.**, **Coudrain, A.**, **Condom, T.**, **Seidel, J.L.**, **Vimeux, F.**, **Moreau, C.**, **Dumoulin, J.P.** and **Lavé, J.** (2011) Lake highstands on the Altiplano (Tropical Andes) contemporaneous with Heinrich 1 and the Younger Dryas: New insights from ^{14}C, U-Th dating and $\delta^{18}O$ of carbonates. *Quat. Sci. Rev.*, **30**, 3973–3989.

Blott, S.J. and **Pye, K.** (2001) Gradistat: A grain size distribution and statistics package for the analysis of unconsolidated sediments. *Earth Surf. Process. Landforms*, **26**, 1237–1248.

Boës, X., **Rydberg, J.**, **Martinez-Cortizas, A.**, **Bindler, R.** and **Renberg, I.** (2011) Evaluation of conservative lithogenic elements (Ti, Zr, Al, and Rb) to study anthropogenic element enrichments in lake sediments. *J. Paleolimnol.*, **46**, 75–87.

Brauer, A. (2004) Annually Laminated Lake Sediments and their Palaeoclimatic Relevance. In: *The climate in historical times*. Springer, Berlin, Heidelberg,109–127.

Burnett, A.P., **Soreghan, M.J.**, **Scholz, C.A.** and **Brown, E.T.** (2011) Tropical East African climate change and its relation to global climate: A record from Lake Tanganyika, Tropical East Africa, over the past 90 kyr. *Palaeogeogr. Palaeoclimatol. Palaeoecol.*, **303**, 155–167.

Camacho, M. and **Kulemeyer, J.J.** (2017) The Quaternary of the Laguna de los Pozuelos Basin, Northern Puna, Argentina. *Springer, Cham*, 237–259.

Carroll, A.R. and **Bohacs, K.M.** (1999) Stratigraphic classification of ancient lakes: Balancing tectonic and climatic controls. *Geology*, **27**, 99–102.

Castino, F., **Bookhagen, B.** and **Strecker, M.R.** (2017) Rainfall variability and trends of the past six decades (1950–2014) in the subtropical NW Argentine Andes. *Clim. Dyn.*, **48**, 1049–1067.

Cheng, H., **Sinha, A.**, **Cruz, F.W.**, **Wang, X.**, **Edwards, R.L.**, **D'Horta, F.M.**, **Ribas, C.C.**, **Vuille, M.**, **Stott, L.D.** and **Auler, A.S.** (2013) Climate change patterns in Amazonia and biodiversity. *Nat. Commun.*, **4**, 1–6.

Clark, P.U., **Dyke, A.S.**, **Shakun, J.D.**, **Carlson, A.E.**, **Clark, J.**, **Wohlfarth, B.**, **Mitrovica, J.X.**, **Hostetler, S.W.** and **McCabe, A.M.** (2009) The Last Glacial Maximum. *Science* **325**, 710–714.

Cohen, A., **McGlue, M.M.**, **Ellis, G.S.**, **Zani, H.**, **Swarzenski, P.W.**, **Assine, M.L.** and **Silva, A.** (2015) Lake formation, characteristics, and evolution in retroarc deposystems: A synthesis of the modern Andean orogen and its associated basins. *Mem. Geol. Soc. Am.*, **212**, 309–335.

Coppo, R. (2015) Estudio de las variaciones hidroclimáticas del Holoceno en el registro sedimentológico de la laguna Lizoite, sierra de Santa Victoria, provincia de Salta. Tesis de Grado, Universidad Nacional de Córdoba, 77pp.

Croudace, I.A.N.W., **Rindby, A.** and **Rothwell, R.G.U.Y.** (2006) ITRAX: description and evaluation of a new multi-function X-ray core scanner. *Geological Society, London, Special Publications*, **267**(1), 51-63.

Cruz, F.W., Burns, S.J., Karmann, I., Sharp, W.D. and **Vuille, M.** (2006) Reconstruction of regional atmospheric circulation features during the late Pleistocene in subtropical Brazil from oxygen isotope composition of speleothems. *Earth Planet. Sci. Lett.*, **248**, 494–506.

Cuven, S., **Francus, P.** and **Lamoureux, S.F.** (2010) Estimation of grain size variability with micro X-ray fluorescence in laminated lacustrine sediments, Cape Bounty, Canadian High Arctic. *J. Paleolimnol.*, **44**, 803–817.

D'Arcy, M., **Schildgen, T.F.**, **Strecker, M.R.**, **Wittmann, H.**, **Duesing, W.**, **Mey, J.**, **Tofelde, S.**, **Weissmann, P.** and **Alonso, R.N.** (2019) Timing of past glaciation at the Sierra de Aconquija, northwestern Argentina, and throughout the Central Andes. *Quat Sci Rev.* **204**, 37-57 doi: 10.1016/j.quascirev.2018.11.022

Davies S., Lamb H. and **Roberts S.** (2015) Micro-XRF Core Scanning in Palaeolimnology: Recent Developments. In: *Micro-XRF Studies of Sediment Cores. Developments in Paleoenvironmental Research* (Eds. Croudace I., Rothwell R.)*, Springer, Dordrecht,* vol 17. https://doi.org/10.1007/978-94-017-9849-5_7

Davison, W. (1993) Iron and manganese in lakes. *Earth Sci. Rev.*, **34**, 119–163.

de Carvalho, L.M.V. and **Cavalcanti, I.F.A.** (2016) The South American Monsoon System (SAMS). In: de Carvalho L., Jones C. (eds) *The Monsoons and Climate Change*. Springer Climate. Springer, Cham. https://doi.org/10.1007/978-3-319-21650-8_6

Einsele, G. (2000) Sequences, Minor Cycles, and Event Stratigraphy. In: *Sedimentary Basins*, *Springer Berlin Heidelberg*, 291–384.

Fagel, N., Pedreros, P., Alvarez, D., Tylmann, W., Namur, O., Da Silva, A.C., Jana, P., Araneda, A., Billy, I., Schmidt, S. and **Urrutia, R.** (2021) Last millennium climate variability of the varved Lake Jeinimeni geochemical record from NE Chilean Patagonia. *Quaternary Science Reviews*, **269**, 107134.

Fernández-Turiel, J.L., Perez–Torrado, F.J., Rodríguez-González, A., Saavedra, J., Carracedo, J.C., Rejas, M., Lobo, A., Osterrieth, M., Carrizo, J.I., Esteban, G., Gallardo, J. and **Ratto, N.** (2019). The large eruption 4.2 ka cal BP in Cerro Blanco, Central Volcanic Zone, Andes: Insights to the Holocene eruptive deposits in the southern Puna and adjacent regions. *Estudios Geológicos*, **75**(1): e088. https://doi.org/10.3989/egeol.43438.515.

Fielding, J.J., Kemp, A.E., Bull, J.M., Cotterill, C.J., Pearce, R.B., Avery, R.S., Langdon, P.G. and **Croudace, I. W.** (2018). Palaeoseismology from microfabric and geochemical analysis of lacustrine sediments, Windermere, UK. *Journal of the Geological Society*, **175**(6), 903-914.

Francus, P., **von Suchodoletz, H.**, **Dietze, M.**, **Donner, R. V.**, **Bouchard, F.**, **Roy, A.J.**, **Fagot, M.**, **Verschuren, D.** and **Kröpelin, S.** (2013) Varved sediments of Lake Yoa (Ounianga Kebir, Chad) reveal progressive drying of the Sahara during the last 6100 years. *Sedimentology*, **60**, 911–934.

Fritz, S.C., **Baker, P.A.**, **Lowenstein, T.K.**, **Seltzer, G.O.**, **Rigsby, C.A.**, **Dwyer, G.S.**, **Tapia, P.M.**, **Arnold, K.K.**, **Ku, T.L.** and **Luo, S.** (2004) Hydrologic variation during the last 170,000 years in the southern hemisphere tropics of South America. *Quat. Res.*, **61**, 95–104.

Garreaud, R.D., **Vuille, M.**, **Compagnucci, R.** and **Marengo, J.** (2009) Present-day South American climate. *Palaeogeogr. Palaeoclimatol. Palaeoecol.*, **281**, 180–195.

Gasparini, G.M., **Rabassa, J.**, **Deschamps, C.** and **Tonni, E.P.** (2016) Introduction. In: Gasparini G., Rabassa J., Deschamps C., Tonni E. (eds) *Marine Isotope Stage 3 in Southern South America, 60 KA B.P.-30 KA B.P.* Springer Earth System Sciences. Springer, Cham. https://doi.org/10.1007/978-3-319-40000-6_1.

Geyh, M., Schotterer, U. and **Grosjean, M.** (1998) Temporal changes of the 14C reservoir effect in lakes. *Radiocarbon* **40**, 921-931.

Geyh, M., Grosjean, M., Núñez, L.A. and **Schotterer, U.** (1999) Radiocarbon reservoir effect and the timing of the Late-Glacial Early Holocene humid phase in the Atacama Desert, Northern Chile. *Quaternary Research* **52**, 143-153.

Gilli, A., **Anselmetti, F.S.**, **Glur, L.** and **Wirth, S.B.** (2013) Lake Sediments as Archives of Recurrence Rates and Intensities of Past Flood Events. In: *Advances in Global Change Research*, *Springer International Publishing*, **47**, 225–242.

Glenn, C.R. and **Kelts, K.** (1991) Sedimentary rhythms in lake deposits. In: *Cycles and Events in Stratigraphy* (Ed. G. Einsele, W. Ricken, and A. Seilacher), Berlin and Heidelberg, 188–221.

González, M.A., Tchilinguirian, P., Pereyra, F., Ramallo, E. and **Gonzalez, O.E.** (2004). Hoja Geológica 2366-IV Ciudad de Libertador General San Martín, provincias de Jujuy y Salta. *SEGEMAR scale 1:250.000*, 1 sheet, 114 pp.

Gottlieb, P., **Wilkie, G.**, **Sutherland, D.**, **Ho-Tun, E.**, **Suthers, S.**, **Perera, K.**, **Jenkins, B.**, **Spencer, S.**, **Butcher, A.** and **Rayner, J.** (2000) Using quantitative electron microscopy for process mineralogy applications. *JOM*, **52**, 24–25.**Grosjean, M.**, **Geyh, M.A.**, **Messerli, B.** and **Schotterer, U.** (1995) Late-glacial and early Holocene lake sediments, ground-water formation and climate in the Atacama Altiplano 22-24°S. *J. Paleolimnol.*, **14**, 241–252.

Grosjean, M., **Van Leeuwen, J.F.N., Van der Knaap, W.O., Geyh, M.A., Ammann, B., Tanner, W., Messerli, B., Núñez, L.A., Valero-Garcés, B.L.,** and **Veit, H**. (2001) A 22,000 ^{14}C year BP sediment and pollen record of climate change from Laguna Miscanti (23 S), northern Chile. *Glob. Planet. Change*, **28**, 35–51.**Grosjean, M.**, **Valero-Garcés, B.L.**, **Geyh, M.A.**, **Messerli, B.**, **Schotterer, U.**, **Schreier, H.** and **Kelts, K.** (1997) Mid- and late-Holocene limnogeology of Laguna del Negro Francisco, northern Chile, and its palaeoclimatic implications. *The Holocene*, **7**, 151–159.

Hajdas, I. (2008) Radiocarbon dating and its applications in Quaternary studies. *Quat. Sci. J.*, **57**, 2–24.

Hardie, L.A., **Smoot, J.P.** and **Eugster, H.P.** (1978) Saline lakes and their deposits: a sediment approach. In *Modern and ancient lake sediments.* Blackwell Oxford, Vol. 2, 7-41 pp.

Hermanns, R.L., Trauth, M.H., Niedermann, S., McWilliams, M. and **Strecker, M.R.** (2000) Tephrochronologic constraints on temporal distribution of large landslides in northwest Argentina. *The Journal of Geology*, **108**(1), 35-52.

Hermanns, R.L. and **Schellenberger, A.** (2008) Quaternary tephrochronology helps define conditioning factors and triggering mechanisms of rock avalanches in NW Argentina. *Quat. Int.*, **178**(1), 261-275.

Hogg, A.G., Heaton, T.J., Hua, Q., Palmer, J.G., Turney, C.S., Southon, J., Bayliss, A., Blackwell, P.G, Boswijk, G., Ramsey, C.B.,Pearson, C., Petchey, F., Reimer, P., Reimer, R. and **Wacker, L.** (2020). SHCal20 Southern Hemisphere calibration, 0–55,000 years cal BP. *Radiocarbon*, 1-20.**Hooper, J.**, **Marx, S.K.**, **May, J.-H.**, **Lupo, L.C.**, **Kulemeyer, J.J.**, **Pereira, E. de los Á.**, **Seki, O.**, **Heijnis, H.**, **Child, D.**, **Gadd, P.** and **Zawadzki, A.** (2020) Dust deposition tracks late-Holocene shifts in monsoon activity and the increasing role of human disturbance in the Puna-Altiplano, northwest Argentina. *The Holocene*, **30**, 519–536.

Hua, Q., **Barbetti, M.** and **Rakowski, A.Z.** (2013) Atmospheric Radiocarbon for the Period 1950–2010. *Radiocarbon*, **55**, 2059–2072.

Kemp, A.E.S. (1996) Laminated sediments as palaeo-indicators. *Geol. Soc. London, Spec. Publ.*, **116**, vii–xii.

Kenis, P., Skurzyński, J., Jary, Z., and **Kubik, R.** (2020) A new methodological approach (QEMSCAN®) in the mineralogical study of Polish loess: Guidelines for further research. *Open Geosciences*, **12**(1), 342-353.

Kock, S.T., **Schittek, K.**, **Wissel, H.**, **Vos, H.**, **Ohlendorf, C.**, **Schäbitz, F.**, **Lupo, L.C.**, **Kulemeyer, J.J.** and **Lücke, A.** (2019) Stable Oxygen Isotope Records (δ^{18}O) of a High-Andean Cushion Peatland in NW Argentina (24° S) Imply South American Summer Monsoon Related Moisture Changes During the Late Holocene. *Front. Earth Sci.*, **7**, 45.

Kylander, M.E., **Ampel, L.**, **Wohlfarth, B.** and **Veres, D.** (2011) High-resolution X-ray fluorescence core scanning analysis of Les Echets (France) sedimentary sequence: New insights from chemical proxies. *J. Quat. Sci.*, **26**, 109–117.

Laskar, J., **Robutel, P.**, **Joutel, F.**, **Gastineau, M.**, **Correia, A.C.M.** and **Levrard, B.** (2004) A long-term numerical solution for the insolation quantities of the Earth. *Astron. Astrophys.*, **428**, 261–285.

Last, W.M. (2002) Geolimnology of salt lakes. *Geosci. J.*, **6**, 347–369.

Liu, X., **Colman, S.M.**, **Brown, E.T.**, **Minor, E.C.** and **Li, H.** (2013) Estimation of carbonate, total organic carbon, and biogenic silica content by FTIR and XRF techniques in lacustrine sediments. *J. Paleolimnol.*, **50**, 387–398.

López Steinmetz, R.L. and **Galli, C.I.** (2015) Hydrological change during the Pleistocene-Holocene transition associated with the Last Glacial Maximum-Altithermal in the eastern border of northern Puna. *Andean Geol.*, **42**, 1–19. **Lupo, L.**, **Kulemeyer, J.J.**, **Torres, G.**, **Oxman, B.** and **Schittek, K.** (2018) Paleoecología del Cuaternario tardío de la Puna del Noroeste argentino. In: S*erie Conservación de la Naturaleza 24. La Puna argentina: naturaleza y cultura*, 54–72.

Lupo, L.C., **Bianchi, M.M.**, **Aráoz, E.**, **Grau, R.**, **Lucas, C.**, **Kern, R.**, **M., C.**, **Tanner, W.** and **Grosjean, M.** (2006) Climate and human impact during the past 2000 years as recorded in the Lagunas de Yala, Jujuy, northwestern Argentina. *Quat. Int.*, **158**, 30–43.

Lynch, K.L., Horgan, B.H., Munakata-Marr, J., Hanley, J., Schneider, R.J., Rey, K.A., Spear, J.R., Jackson, W.A., and Ritter, S.M. (2015) Near-infrared spectroscopy of lacustrine sediments in the Great Salt Lake Desert: An analog study for Martian paleolake basins, *J. Geophys. Res. Planets*, **120**, 599–623, doi:10.1002/2014JE004707

Mangili, C., Brauer, A., Moscariello, A., and Naumann, R. (2005) Microfacies of detrital event layers deposited in Quaternary varved lake sediments of the Piànico-Sèllere Basin (northern Italy). *Sedimentology*, **52**, 5, 927-943.

Martin-Puertas, C., **Brauer, A.**, **Dulski, P.** and **Brademann, B.** (2012) Testing climate-proxy stationarity throughout the Holocene: An example from the varved sediments of Lake Meerfelder Maar (Germany). *Quat. Sci. Rev.*, **58**, 56–65.

Martin-Puertas, C., **Brauer, A.**, **Wulf, S.**, **Ott, F.**, **Lauterbach, S.** and **Dulski, P.** (2014) Annual proxy data from Lago Grande di Monticchio (southern Italy) between 76 and 112 ka: New chronological constraints and insights on abrupt climatic oscillations. *Clim. Past*, **10**, 2099–2114.

Martini, M.A., **Kaplan, M.R.**, **Strelin, J.A.**, **Astini, R.A.**, **Schaefer, J.M.**, **Caffee, M.W.** and **Schwartz, R.** (2017a) Late Pleistocene glacial fluctuations in Cordillera Oriental, subtropical Andes. *Quat. Sci. Rev.*, **171**, 245–259.

Martini, M.A., **Strelin, J.A.**, **Flores, E.**, **Astini, R.A.** and **Kaplan, M.R.** (2017b) Recent climate warming and the Varas rock glacier activity, Cordillera Oriental, Central Andes of Argentina. *GeoResJ*, **14**, 67–79.

McGlue, M.M., **Cohen, A.S.**, **Ellis, G.S.** and **Kowler, A.L.** (2013) Late Quaternary stratigraphy, sedimentology and geochemistry of an underfilled lake basin in the Puna plateau (northwest Argentina). *Basin Res.*, **25**, 638–658.

McGlue, M.M., **Palacios-Fest, M.R.**, **Cusminsky, G.C.**, **Camacho, M.**, **Ivory, S.J.**, **Kowler, A.L.** and **Chakraborty, S.** (2017) Ostracode Biofacies and Shell Chemistry Reveal Quaternary Aquatic Transitions in the Pozuelos Basin (Argentina). *Palaios*, **32**, 413–428.

Melles, M., **Brigham-Grette, J.**, **Minyuk, P.S.**, **Nowaczyk, N.R.**, **Wennrich, V.**, **DeConto, R.M.**, **Anderson, P.M.**, **Andreev, A.A.**, **Coletti, A.**, **Cook, T.L.**, **Haltia-Hovi, E.**, **Kukkonen, M.**, **Lozhkin, A. V.**, **Rosén, P.**, **Tarasov, P.**, **Vogel, H.** and **Wagner, B.** (2012) 2.8 Million years of arctic climate change from Lake El'gygytgyn, NE Russia. *Science*, **337**, 315–320.

Morales, M.R., **Bustos, S.** and **Maidana, N.I.** (2015) Registro de diatomeas de los últimos 1400 años de la Laguna Pululos, Jujuy, Argentina. *Ecol. Austral*, **25**, 182–191.

Morlock, M.A.; Vogel, H.; Russell, J.M.; Anselmetti, F.S.; Bijaksana, S. (2021). Quaternary environmental

changes in tropical Lake Towuti, Indonesia, inferred from end-member modelling of X-ray fluorescence core-scanning data. *Journal of Quaternary Science* **36**(6), 1040-1051. Wiley 10.1002/jqs.3338 .

Naeher, S., **Gilli, A.**, **North, R.P.**, **Hamann, Y.** and **Schubert, C.J.** (2013) Tracing bottom water oxygenation with sedimentary Mn/Fe ratios in Lake Zurich, Switzerland. *Chem. Geol.*, **352**, 125–133.

Neugebauer, I., **Schwab, M.J.**, **Waldmann, N.D.**, **Tjallingii, R.**, **Frank, U.**, **Hadzhiivanova, E.**, **Naumann, R.**, **Taha, N.**, **Agnon, A.**, **Enzel, Y.** and **Brauer, A.** (2015) Hydroclimatic variability in the Levant during the early last glacial (117–75 ka) derived from micro-facies analyses of deep Dead Sea sediments. *Clim. Past Discuss.*, **11**, 3625–3663.

Neugebauer, I., **Schwab, M.J.**, **Waldmann, N.D.**, **Tjallingii, R.**, **Frank, U.**, **Hadzhiivanova, E.**, **Naumann, R.**, **Taha, N.**, **Agnon, A.**, **Enzel, Y.** and **Brauer, A.** (2016) Hydroclimatic variability in the Levant during the early last glacial (~117-75 ka) derived from micro-facies analyses of deep Dead Sea sediments. *Clim. Past*, **12**, 75–90.

Neugebauer, I., **Thomas, C.**, **Waldmann, N.**, **Recasens, C.** and **Ariztegui, D.** Cyclic preservation of Fe/Mn-redox fronts in sediments of an oligotrophic, ventilated deep-water lake (Lago Fagnano, Tierra del Fuego). doi: 10.31223/OSF.IO/MJDYF

Noble, P.J., **Ball, G.I.**, **Zimmerman, S.H.**, **Maloney, J.**, **Smith, S.B.**, **Kent, G.**, **Adams, K.D.**, **Karlin, R.E.** and **Driscoll, N.** (2016) Holocene paleoclimate history of Fallen Leaf Lake, CA., from geochemistry and sedimentology of well-dated sediment cores. *Quat. Sci. Rev.*, **131**, 193–210.

Novello, V.F., **Cruz, F.W.**, **Vuille, M.**, **Stríkis, N.M.**, **Edwards, R.L.**, **Cheng, H.**, **Emerick, S.**, **De Paula, M.S.**, **Li, X.**, **Barreto, E.D.S.**, **Karmann, I.** and **Santos, R. V.** (2017) A high-resolution history of the South American Monsoon from Last Glacial Maximum to the Holocene. *Sci. Rep.*, **7**, 1–8.

Nunnery, J.A., **Fritz, S.C.**, **Baker, P.A.** and **Salenbien, W.** (2019) Lake-level variability in Salar de Coipasa, Bolivia during the past ~40,000 yr. *Quat. Res. (United States)*, **91**, 829–847.

Palacios, D., **Stokes, C.R.**, **Phillips, F.M.**, **Clague, J.J.**, **Alcalá-Reygosa, J.**, **Andrés, N.**, **Angel, I.**, **Blard, P.H.**, **Briner, J.P.**, **Hall, B.L.**, **Dahms, D.**, **Hein, A.S.**, **Jomelli, V.**, **Mark, B.G.**, **Martini, M.A.**, **Moreno, P.**, **Riedel, J.**, **Sagredo, E.**, **Stansell, N.D.**, **Vázquez-Selem, L.**, **Vuille, M.** and **Ward, D.J.** (2020) The deglaciation of the Americas during the Last Glacial Termination. *Earth-Science Rev.*, **203**, 103113.

Peinerud, E.K. (2000) Interpretation of Si concentrations in lake sediments: three case studies. *Environ. Geol.*, **40**, 64–72.

Pełechaty, M., **Pukacz, A.**, **Apolinarska, K.**, **Pełechata, A.** and **Siepak, M.** (2013) The significance of Chara vegetation in the precipitation of lacustrine calcium carbonate. *Sedimentology*, **60**, 1017–1035.

Pfeiffer, M., Latorre, C., Santoro, C. M., Gayo, E.M., Rojas, R., Carrevedo, M.L., McRostied, V.B., Finstad, K.M., Heimsath, A., Jungers, M.C., De Pol-Holz, R. and **Amundson, R**., (2018) Chronology, stratigraphy and hydrological modelling of extensive wetlands and paleolakes in the hyperarid core of the Atacama Desert during the late quaternary. *Quaternary Science Reviews*, **197**, 224-245.

Placzek, C., **Quade, J.** and **Patchett, P.J.** (2006) Geochronology and stratigraphy of late Pleistocene lake cycles on the southern Bolivian Altiplano: Implications for causes of tropical climate change. *Bull. Geol. Soc. Am.*, **118**, 515–532.

Placzek, C., Quade, J., Rech, J.A., Patchett, P.J., and **de Arce, C.P.** (2009). Geochemistry, chronology and

stratigraphy of Neogene tuffs of the Central Andean region. *Quaternary Geochronology*, **4**(1), 22-36.

Quade, J., **Rech, J.A.**, **Betancourt, J.L.**, **Latorre, C.**, **Quade, B.**, **Rylander, K.A.** and **Fisher, T.** (2008) Paleowetlands and regional climate change in the central Atacama Desert, northern Chile. *Quat. Res.*, **69**, 343–360.**Renaut, R.** and **Gierlowski-Kordesch, E.** (2010) Lakes. In: *Facies Model*, 4th Ed (Ed. N. James and R. Dalrymple), *Geological Association of Canada*, Toronto, 541–575.

Sampietro-Vattuone, M.M., Báez, W.A., Peña-Monné, J.L. and **Sola, A.** (2020) Chronological and geomorphological approach to the Holocene tephras from Tafí and Santa María valleys, NW Argentina. *Quaternary Research*, **94**, 14-30.

Schäbitz, F., **Lupo, L.**, **Kulemeyer, J.A.** and **Kulemeyer, J.J.** (2001) Variaciones en la vegetación, el clima y la presencia humana en los últimos 15.000 años en el borde oriental de la Puna, provincias de Jujuy y Salta, noroeste argentino. *Asoc. Paleontológica Argentina, Publicación Espec.*, **8**, 155–162.

Schildgen, T.F., **Robinson, R.A.J.**, **Savi, S.**, **Phillips, W.M.**, **Spencer, J.Q.G.**, **Bookhagen, B.**, **Scherler, D.**, **Tofelde, S.**, **Alonso, R.N.**, **Kubik, P.W.**, **Binnie, S.A.** and **Strecker, M.R.** (2016) Landscape response to late Pleistocene climate change in NW Argentina: Sediment flux modulated by basin geometry and connectivity. *J. Geophys. Res.: Earth Surface*, **121**(2), 392-414.

Schillereff, D.N., **Chiverrell, R.C.**, **Macdonald, N.** and **Hooke, J.M.** (2014) Flood stratigraphies in lake sediments: A review. *Earth-Science Rev.*, **135**, 17–37.

Schittek, K., **Kock, S.T.**, **Lücke, A.**, **Hense, J.**, **Ohlendorf, C.**, **Kulemeyer, J.J.**, **Lupo, L.C.** and **Schäbitz, F.** (2016) A high-altitude peatland record of environmental changes in the NW Argentine Andes (24 ° S) over the last 2100 years. *Clim. Past*, **12**, 1165–1180.

Schittek, K., **Kock, S.T.**, **Lücke, A.**, **Ohlendorf, C.**, **Kulemeyer, J.J.**, **Lupo, L.C.** and **Schäbitz, F.** (2015) Environmental and climatic history in the NW Argentine Andes (24° S) over the last 2100 years inferred from a high-altitude peatland record. *Clim. Past Discuss.*, **11**, 2037–2076.

Schlolaut, G., **Brauer, A.**, **Marshall, M.H.**, **Nakagawa, T.**, **Staff, R.A.**, **Bronk Ramsey, C.**, **Lamb, H.F.**, **Bryant, C.L.**, **Naumann, R.**, **Dulski, P.**, **Brock, F.**, **Yokoyama, Y.**, **Tada, R.** and **Haraguchi, T.** (2014) Event layers in the Japanese Lake Suigetsu "SG06" sediment core: Description, interpretation and climatic implications. *Quat. Sci. Rev.*, **83**, 157–170.

Schnurrenberger, D., **Schnurrenberger, D.**, **Russell, J.**, **Russell, J.**, **Kelts, K.** and **Kelts, K.** (2003) Classification of lacustrine sediments based on sedimentary components 1, 1,2 † 1. *J. Paleolimnol.*, 141–154.

Šegvić, B., Girardclos, S., Zanoni, G., González, C. A., Steimer-Herbet, T., and **Besse, M.** (2018). Origin and paleoenvironmental significance of FeMn nodules in the Holocene perialpine sediments of Geneva Basin, western Switzerland. *Applied Clay Science*, **160**, 22-39.

Stojakowits, P., Mayr, C., Ivy-Ochs, S., Preusser, F., Reitner, J. M., and **Spötl, C.** (2021) Environments at the MIS 3/2 transition in the northern Alps and their foreland. *Quaternary International*, **581**, 99-113.

Sylvestre, M., Servant, M., Servant-Vildary, S., Causse, C., Fournier, M. and **Ybert, J.-P.** (1999) Lake level chronology on the Southern Bolivian Altiplano (18°-23°S) during Late-Glacial Time and the Early Holocene. *Quaternary Research* **51**, 54-66.

Synal, H. A., Stocker, M., and Suter, M. (2007) MICADAS: A new compact radiocarbon AMS system. *Nuclear*

Instruments & Methods in Physics Research Section B-Beam Interactions with Materials and Atoms, **259** (1), 7-13.

Tchilinguirian, P. and **Morales, M.R.** (2013) Mid-Holocene paleoenvironments in Northwestern Argentina: Main patterns and discrepancies. *Quat. Int.*, **307**, 14–23.

Tofelde, S., **Schildgen, T.F.**, **Savi, S.**, **Pingel, H.**, **Wickert, A.D.**, **Bookhagen, B.**, **Wittmann, H.**, **Alonso, R.N.**, **Cottle, J.** and **Strecker, M.R.** (2017) 100 kyr fluvial cut-and-fill terrace cycles since the Middle Pleistocene in the southern Central Andes, NW Argentina. *Earth Planet. Sci. Lett.*, **473**, 141–153.

Torres, G.R., **Lupo, L.C.**, **Kulemeyer, J.J.** and **Pérez, C.F.** (2016) Palynological evidence of the geoecological belts dynamics from Eastern Cordillera of NW Argentina (23° S) during the Pre-Last Glacial Maximum. *Andean Geol.*, **43**, 151–165.

Trauth, M.H., **Bookhagen, B.**, **Marwan, N.** and **Strecker, M.R.** (2003) Multiple landslide clusters record Quaternary climate changes in the northwestern Argentine Andes. *Palaeogeogr. Palaeoclimatol. Palaeoecol.*, **194**, 109–121.

Trauth, M.H. and **Strecker, M.R.** (1999) Formation of landslide-dammed lakes during a wet period between 40,000 and 25,000 yr B.P. in northwestern Argentina. *Palaeogeogr. Palaeoclimatol. Palaeoecol.*, **153**, 277–287.

Valero-Garcés, B.L., Delgado-Huertas, A., Navas, A. and **Ratto, N.** (1999). Large ^{13}C enrichment in primary carbonates from Andean Altiplano lakes, Northwest Argentina. *Earth Planet. Sci. Lett.,* **171**, 253–266.

Valero-Garcés, B., **Delgado-Huertas, A.**, **Ratto, N.**, **Navas, A.** and **Edwards, L.** (2000) Paleohydrology of Andean saline lakes from sedimentological and isotopic records, Northwestern Argentina. *J. Paleolimnol.*, **24**, 343–359.

van der Meer, J.J., and Menzies, J. (2011). The micromorphology of unconsolidated sediments. *Sedimentary Geology*, **238**(3-4), 213-232.

Vera, C. (2006) Towards a unified view of the American Monsoon System. *J. Clim.*, **19**, 5000.

Viale, M., **Bianchi, E.**, **Cara, L.**, **Ruiz, L.E.**, **Villalba, R.**, **Pitte, P.**, **Masiokas, M.**, **Rivera, J.** and **Zalazar, L.** (2019) Contrasting Climates at Both Sides of the Andes in Argentina and Chile. *Front. Environ. Sci.*, **7**, 69.

Vogel, H., **Wagner, B.**, **Zanchetta, G.**, **Sulpizio, R.** and **Rosén, P.** (2010) A paleoclimate record with tephrochronological age control for the last glacial-interglacial cycle from Lake Ohrid, Albania and Macedonia. *J. Paleolimnol.*, **44**, 295–310.

Waldmann, N., **Anselmetti, F.S.**, **Ariztegui, D.**, **Austin, J.A.**, **Pirouz, M.**, **Moy, C.M.** and **Dunbar, R.** (2011) Holocene mass-wasting events in Lago Fagnano, Tierra del Fuego (54°S): Implications for paleoseismicity of the Magallanes-Fagnano transform fault. *Basin Res.*, **23**, 171–190.

Wang, X., **Auler, A.S.**, **Edwards, R.L.**, **Cheng, H.**, **Ito, E.**, **Wang, Y.**, **Kong, X.** and **Solheid, M.** (2007) Millennial-scale precipitation changes in southern Brazil over the past 90,000 years. *Geophys Res Lett.* **34** doi: 10.1029/2007GL031149

Weltje, G.J. and **Tjallingii, R.** (2008) Calibration of XRF core scanners for quantitative geochemical logging of sediment cores: Theory and application. *Earth Planet. Sci. Lett.*, **274**, 423–438.

Wetzel, R.G. (2001) Iron, Sulfur, and Silica cycles. In: *Limnology*, *Elsevier*, 289–330.

Wilhelm, B., **Arnaud, F.**, **Sabatier, P.**, **Magand, O.**, **Chapron, E.**, **Courp, T.**, **Tachikawa, K.**, **Fanget, B.**, **Malet, E.**, **Pignol, C.**, **Bard, E.** and **Delannoy, J.J.** (2013) Palaeoflood activity and climate change over the last 1400 years recorded by lake sediments in the north-west European Alps. *J. Quat. Sci.*, **28**, 189–199.

Wulf, S., **Ott, F.**, **Słowiński, M.**, **Noryśkiewicz, A.M.**, **Dräger, N.**, **Martin-Puertas, C.**, **Czymzik, M.**, **Neugebauer, I.**, **Dulski, P.**, **Bourne, A.J.**, **Błaszkiewicz, M.** and **Brauer, A.** (2013) Tracing the Laacher See Tephra in the varved sediment record of the Trzechowskie palaeolake in central Northern Poland. *Quat. Sci. Rev.*, **76**, 129–139.

Zech, J., **Zech, R.**, **Kubik, P.W.** and **Veit, H.** (2009) Glacier and climate reconstruction at Tres Lagunas, NW Argentina, based on ^{10}Be surface exposure dating and lake sediment analyses. *Palaeogeogr. Palaeoclimatol. Palaeoecol.*, **284**, 180–190.

Zhou, J. and **Lau, K.M.** (1998) Does a monsoon climate exist over South America? *J. Clim.*, **11**, 1020–1040.

Zolitschka, B., **Francus, P.**, **Ojala, A.E.K.** and **Schimmelmann, A.** (2015) Varves in lake sediments - a review. *Quat. Sci. Rev.*, **117**, 1–41.

FIGURE CAPTIONS

Fig. 1. Study area in the subtropical Andes from North-western Argentina. (**A**) Precipitation map of the subtropical Andes and surrounding area. The red square denotes the extension of (B). (**B**) Digital Elevation Model (DEM) of the north-western Argentina with the location of Laguna La Salada Grande (LSG). BC: Botuverá Cave, SU: Salar de Uyuni, Alt: Altiplano, LG: Laguna Guayatayoc, LP: Laguna Pozuelos, SG: Salinas Grades.

Fig. 2. Geomorphic setting of the Laguna La Salada Grande (LSG) system. (**A**) Watershed of LSG and Laguna La Salada Chica (LSC) with the main geomorphic features (satellite imagery from 07/27/2018; source ESRI™, DigitalGlobe). (**B**) Zoom to LSG area with the location of the retrieved sediment cores (LSG1 and LSG2) and outcrops (O1, O2 and O3) shown in Fig. 3. (**C**) and (**D**) Field photographs showing retrieval of the LSG1 and LSG2 cores, respectively.

Fig. 3. Topographic profile and general stratigraphy reconstructed from outcrops in the LSG watershed (see Fig. 2 for location). (**A**) Schematic downstream profile of the outcrops and location of the core sites. The horizontal scale shows the straight distance to LSG1 site (Fig. 1B). The red dashed line marks the position of the white ash along the stratigraphy. (**B**) to (**D**) Stratigraphy, photograph and sedimentary column of outcrops 1, 2 and 3, including lithology and grain size, their correlation based on the stratigraphic position (black dashed lines), and a broad palaeoenvironmental interpretation of the strata. Algal (macrophyte) remains in outcrop 1 present infinite radiocarbon ages (Table 1). Outcrops 1 and 2 correspond to the same gully. Outcrop 3 corresponds to a terrace scarp. The coloured shadow connecting the columns represents the stratigraphic position of the white ash bed.

Fig. 4. Multiproxy results and photographs of the Laguna La Salada Grande (LSG) deposits. (**A**) LSG1 core. (**B**) The volcanic ash layer section at the outcrop 3 (Fig. 3D). Elemental counts were obtained in this case through micro-XRF line measurements. (**C**) LSG2 core. Measured parameters include: calibrated ages (ka = calibrated 1000 years before 1950), magnetic susceptibility (MS, in SI units), mean particle size (in micrometres), percentage composed by medium silt to fine sand (Si+Sa%), XRF counts (or micro-XRF counts in the white ash) of Fe, K, Ca, S and Mn, Zr/Ti log ratio, and total organic (TOC) and inorganic carbon (TIC) percentages. At the top of the figure the parameters were grouped according to the general proxies they represent

(grain size, lithogenic elements, bioclasts – organic matter and oxygen conditions). Sedimentary units and subunits (UA, UB1, UB2, UC, UD and UE) are included next to the sediment photographs. The grey shadows indicate the presence of a dark tephra. The blue parallel lines shaping double 'M' represent possible discontinuities in this study's records. The bottom part of LSG2 core (UD and UE) was selected for microfacies analyses shown in Fig. 6.

Fig. 5. Principal component analyses (PCA). (**A**) Biplot of the 2 principal components (PC1 and PC2) including samples from LSG1 and LSG2 cores. Circles represent samples (according to the XRF measurement interval), and different colours represent units and subunits. The length of the arrow indicates the element or ratio contribution to the variance. (**B**) PCA for unit D. (**C**) PCA for unit E. The grey text above the images in (**B**) and (**C**) indicate different groups of proxies according to the distribution of the elements and elemental ratios along the axes.

Fig. 6. Microfacies (MF) images in units E and D (see text for names and Table 1 for characterization). (**A**) Photograph showing intercalation of MF1 and MF2 in unit E. Notice the bioturbation structure in MF1 at 137 cm depth. (**B**) Microscopic image showing non preferentially oriented ostracod valves and algae fragments (charophytes) in MF2 and clayey MF1 in unit E. Notice the normal grading from MF2 to MF1 (**C**) Smear slide of MF1 showing diatoms, an amber volcanic fragment and organic matter (OM) aggregates. Very small framboidal crystals of pyrite are observed inside the diatom valve and in the OM aggregate. (**D**) Smear slide of MF2 showing large ostracod fragments (>100 μm) associated with dark amorphous organic matter and clay. (**E**) Photograph of ochre MF3 intercalated with MF4 in unit D. (**F**) Microscopic image of MF3 showing cracked structures filled with sediments of MF2. Internal microlamination in MF3 and wedge-shaped detritus from MF2 can be visualized. (**G**) Microscopic image of a MF4, MF3 and MF1 intercalation. Lower and upper halves of the section show different bedding angles. MF3 is composed of very fine-grained material with diatoms preferentially settled at the bottom and the top of the lamina. Heavier sandy silts from MF4 deform the underlaying soft and saturated MF3 muds, which form flame structures showing a preferential orientation related to palaeoslope. In MF1 ostracod valves are oriented parallel to lamination. Grey triangles denote vertical normal grading. (**H**) MF3 smear slide where different ochre-coloured diatoms are recognized. (**I**) Smear slide of MF4 showing sands composed mainly of inorganic angularly shaped minerals and intraclasts, glass shards and carbonate fragments. (**J**) Photograph of a MF5 discrete lamina in unit

D. (**K**) Microscopic image of a smear slide of MF5 under plane polarized light showing a very fine-grained matrix and diatoms. This sample was taken from the discrete white carbonate-rich lamina. (**L**) Microscopic image of MF5 (same frame as **K**) under crossed polarized light highlighting clays and an aragonitic composition with acicular-like to rice-like texture of the matrix.

Fig. 7. Microfacies analyses in sediments from units D and E from core LSG2. (**A**) X-ray fluorescence (XRF) counts of Ca, Fe and S in laminated and banded sectors of units D and E. (**B**) Detailed photographs of unit E and D sediments (same depth interval as **A**). The dashed rectangle marks the micro-XRF map shown in (**G**) and (**H**). (**C**) Thin sections of selected areas (light blue shadows) of the cores under plane polarized light and the correspondent microfacies. Four of the five identified microfacies are present in this figure. (**D**) Mineralogical QEMSCAN maps of parts of the thin sections. (**E**) and (**F**) illustrate details of mineralogical composition in units D and E, respectively. Circles mark special mineral composition in the maps. Average map surface percentage of the total mapped areas are shown in the legend. (**G**) and (**H**) Micro-XRF elemental maps, where the relative intensity of colours is associated with the micro-XRF counts of every element (i.e. brighter colours meaning higher counts as shown in the legend).

Fig. 8. Comparison of the Laguna La Salada Grande (LSG) record with other palaeoclimatic proxies in South America during marine isotopic stages (MIS) 1, 2 and 3 (see Fig. 1 for location). Boxes at the top of the figure indicate the timing of MIS and the Last Glacial Maximum (LGM). (**A**) $\delta^{18}O$ speleothem record from Botuverá cave, south-eastern Brazil (Wang *et al*., 2007), as a proxy of palaeoprecipitation and January insolation at 30°S (Laskar *et al*., 2004). (**B**) Natural gamma radiation, which is a proxy for effective moisture, with the stratigraphy of the Salar de Uyuni drill core (Fritz *et al*., 2004). (**C**) Chronology of the glacial expansions around Nevado de Chañi massif, North-western Argentina (Martini *et al*., 2017a). (**D**) Interpretative scheme of the depositional processes that affected LSG and its watershed as the coarse detrital influx to the lake (based on the textural medium silt to sand and Zr/Fe data, and the Ca peaks of XRF). High-energy discharges detected period is indicated for units D and E. A lake level drop and fluvial incision occurred at an undetermined time between subunit B1, and unit A is marked as a dashed line. (**E**) Schematic environmental reconstruction of LSG interpreted based on the sedimentary units and microfacies analysis, including the oxygenation conditions (based on the S and Mn data), the

relative lake level and the lake environmental zones (profundal or open water, intermediate, and littoral/sublittoral environment). (**F**) Sedimentary units of LSG. The vertical light grey line points the white volcanic ash marker. The angular vertex towards the right-end of unit E indicates that its base was not reached and has an infinite radiocarbon age (see Table 1).

Table 1. Accelerator mass spectrometry (AMS) dating corresponding to LSG2 and LSG1 cores, and gully outcrop 1 measured at the ETH laboratory. Asterisks indicate rejected (*) or uncalibrated infinite ages (**). a - refers to the depth below the top of the gully.

Table 2. Microfacies (MF) characterization, description and interpretation.

Appendix S1. Chronology based on preliminary ^{210}Pb and ^{137}Cs radioisotope dating of the recent sediments from Laguna La Salada Grande, North-western Argentina. The methodology, a supplementary figure (Fig. S1), and the main results of the measurements, as well as the specific literature, are described in this appendix.

Fig. S1. Preliminary radioisotope dating of recent sediments from core LSG1 at Laguna La Salada Grande. (**A)** Profile of unsupported ^{210}Pb ($^{210}Pb_{xs}$) activity and uncertainty in Becquerel per kilogram. Orange shadow shows the portion of sediments where $^{210}Pb_{xs}$ was no longer detected. (**B)** Profile of ^{137}Cs and uncertainty in Becquerel per kilogram showing the maximum peak of activity at 10 cm depth corresponding to 1963 CE for the Southern Hemisphere (UNSCEAR, 2000). (**C)** Linear sedimentation rates considering the 1963 CE ^{137}Cs maximum detection level at 10 cm depth (dashed line) and the constant flux ^{210}Pb model (continuous line). Sedimentary units A and B are delimited to the right.

Table 1

Lab code	Core/ outcrop	Depth (cm)	Material	^{14}C age BP	±1σ	δ^{13}C (‰)	C/N	Median Probability	1 σ range		2 σ range	
									Calibrated years BP (before 1950)/ CE			
									Lower	Upper	Lower	Upper
ETH-91213	LSG1	2	Carbonates (shells)	-177	22	-16.2	–	*1956 CE*	*1956.5 CE*	*1957.1 CE*	*1956.2 CE*	*1957.4 CE*
									1956.2 CE	*1956.3 CE*		
ETH-91214	LSG1	147	Bulk sediment	17361	64	-24.8	2.3	20900	20832	21968	20697	21090
ETH-91208	LSG2	8	Bulk sediments	18759	66	-19.6	4.32	22656	22499	22785	22445	22902
ETH-91209	LSG2	123	Carbonates (shells)	29737	130	-5.5	–	34261	34145	34390	33984	34493
ETH-91217*, **	LSG2	123	Bulk organic matter	>45500	–	-14.8	6.52					
ETH-91210**	LSG2	145	Organic macro-remains	>47300	–	-18.5	165.07					
ETH-91211**	Outcrop 1	250[a]	Macro fossils	>45300	–	-17.0	81.59					

Table 1. AMS dating corresponding to LSG2 and LSG1 cores, and gully outcrop 1 measured at the ETH laboratory. Asterisks indicate rejected (*) or uncalibrated infinite ages (**). [a] Refers to the depth below the top of the gully.

Table 2. Microfacies (MF) characterization, description and interpretation.

Microfacies	Characteristics	Description	Depositional environment
MF1. *Dark grey, organic matter-rich silts*	**Colour**: dark grey to medium grey. **Structure:** massive with transitional basal contact. **Components**: detrital coarse minerals, amorphous organic matter, clays, diatoms, ostracod valves, charophyte fragments. **Mineralogy:** illite, quartz, plagioclase, and minor amounts of montmorillonite, biotite, K-feldespar, muscovite, pyrite and traces of gypsum. **Laminae thickness**: 2 mm to 1 cm. **Texture**: polymodal to bi-modal (4 µm and 31 µm); mud (matrix), coarsed-silt sized bioclasts, poorly sorted. **Chemistry**: Fe and Si-rich, S present in some layers.	Distributed along units D and E. The most abundant microfacies along unit E. It lacks internal structures and is formed by an abundant clayey matrix (>80%) with coarse-silt-sized biogenic and mineral components, in different proportions (Fig. 6A, B, C, F and G). Fe contribution associated to illite minerals (Fig. 7D to F). Pyrite is present in unit E in framboidal form inside the diatoms and around organic matter (Fig. 7F). Burrows observed in a MF1 layer at unit E indicate localized bioturbation (Fig. 6A).	Profundal to intermediate lake areas in a relatively deep lake. Low energy environment, subaqueous sedimentation in an organic-matter productive lake with periods of low bottom oxygenation. Pyrite possibly associated to bacterial reduction of organic matter.
MF2. *Brown bioclastic carbonate oozes*	**Colour**: greyish brown. **Structure**: undulated and irregular lamination with sharp basal contacts. Some of the laminae show normal grading. **Components**: carbonate bioclasts (ostracods, charophyte fragments), diatom frustules and lithogenic grains, variable fine-grained matrix, organic matter and clay aggregates. **Mineralogy**: calcite–aragonite, quartz, biotite, plagioclase and minor amounts of pyrite. **Laminae thickness**: 0.3 mm to 1 cm. **Texture**: medium to coarse silt and sandy silt (polymodal, with a main mode of 44 µm), very poorly sorted, bioclasts ≥1 mm. **Chemistry**: Ca-rich.	Found along units E and D, intercalated with MF1 (Fig. 6A, B, D and G). It is mainly composed by large calcite/aragonite bioclasts, sometimes parallelly oriented to the lamination (Fig. 7H). Variable matrix formed by siliciclasts, OM and clay aggregates. Few charophyte fragments (Fig. 6B) are present (much less abundant in unit D than in unit E). In unit E, minor amounts of pyrite can be found inside or covering the internal walls of bioclasts or as small framboidal opaque pyrite.	Carbonate-rich water. Littoral to profundal lake environments, accumulation formed by sporadic higher energy transporting bioclastic material and variable amounts of siliciclasts from littoral areas.
MF3. *Ochre clayey*	**Colour**: ochre.	Ddistributed along unit D (Fig. 6E), showing normal	Shallow water column and low energy

muds	**Structure**: undulated laminated with sharp contacts, presence of cracks and localized soft sediment deformation caused by loading. Internal microlamination is recognized in some laminae. Internal grading is usual. **Components**: clayey matrix, diatom valves, and organic matter. **Mineralogy**: illite, quartz and unidentified material. **Laminae thickness**: <0.3 mm to 5 mm. **Texture**: fine silt to clay (unimodal, mean *ca* 9 µm). **Chemistry**: Fe, K and Si-rich.	and reverse internal grading. It has an illite-rich composition, with abundant unidentified material fringing some of these laminae (Fig. 7E). Important amounts of diatoms concentrate in bands at the base and/or the top of this microfacies (Fig. 6G). In discrete laminae, crack structures can be recognized (Fig. 6F). It is frequently found deformed by heavier sandy microfacies (for example, MF4; Fig. 6G).	conditions, in well-oxygenated environments with variable water availability. Littoral or sublittoral environment subject to sporadically load deformation. Yellow colour is associated to oxidation of Fe in illite. Diatom bloom events are preserved.
MF4. *Dark grey sandy silts*	**Colour**: dark grey. **Structure**: massive, discontinuous to irregular wedge-shaped lamination causing loading structures. **Components**: detrital coarse grains. **Mineralogy**: plagioclase, quartz, biotite, illite aggregates, calcite and K-feldespar. **Laminae thickness**: irregular (between 1 mm and 5 mm). **Texture**: medium to sandy silts (bimodal, mean *ca* 20 to 34 µm). **Chemistry**: Si, Fe and Ca-rich.	Mostly found in unit D. Irregularly shaped microfacies (wedge shaped), sometimes discontinuous, internally massive (Fig. 6G and I). Some laminae induce loading structures in the underlying softer sediments generating irregular and oblique contacts (Fig. 6G).	Open water to littoral environments, in shallow-water conditions. Lithoclasts reflecting high-energy events carrying allochthonous material from the watershed to the lake.
MF5. *White carbonate muds*	**Colour**: white. **Structure**: thick laminae, internally massive, with sharp contacts. **Composition**: detrital and carbonate minerals, and diatom valves **Mineralogy**: aragonite, calcite and biotite. **Laminae thickness**: 3 mm to 1 cm. **Texture**: unimodal fine silt (*ca* 10 µm), poorly sorted. **Chemistry**: Ca-rich.	Isolated homogeneous laminae with sharp contacts randomly distributed along unit D (Fig. 6J). Internally massive. The minerals have acicular forms, indicative of aragonite (Fig. 6K and L).	Chemical carbonate precipitation (biologically induced?) in open water areas and low energy environments.

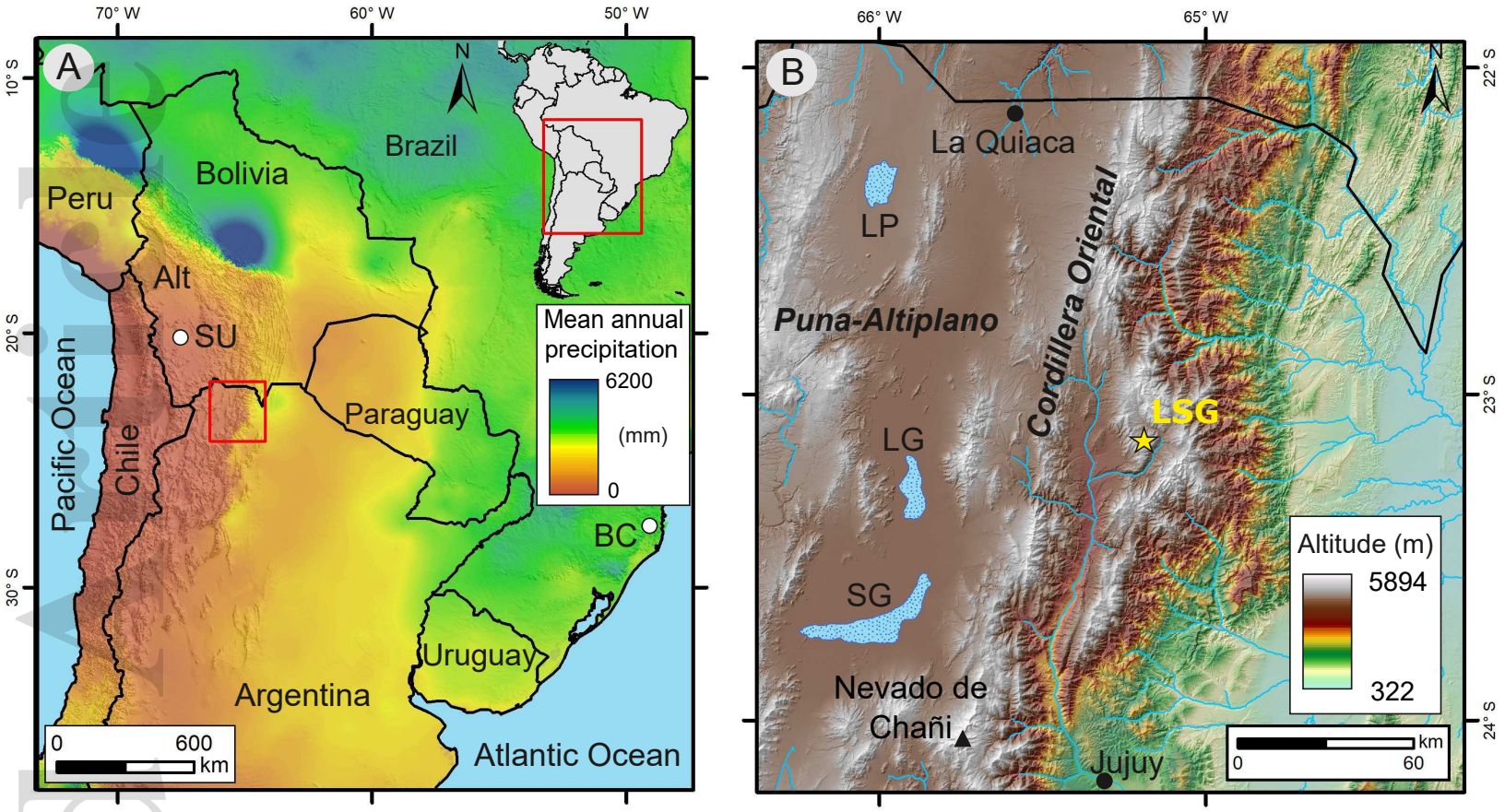

sed_13004_f1.eps

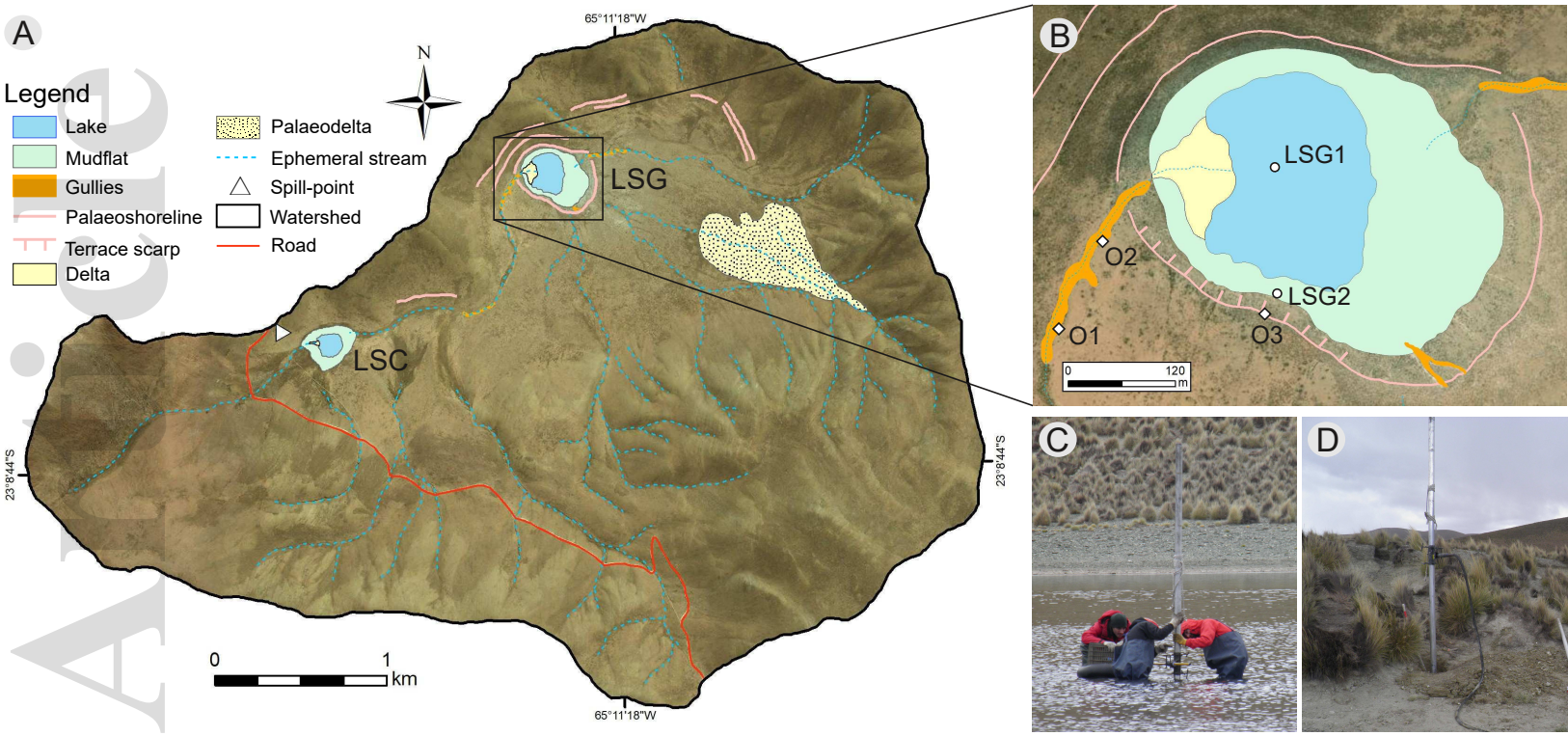

sed_13004_f2.eps

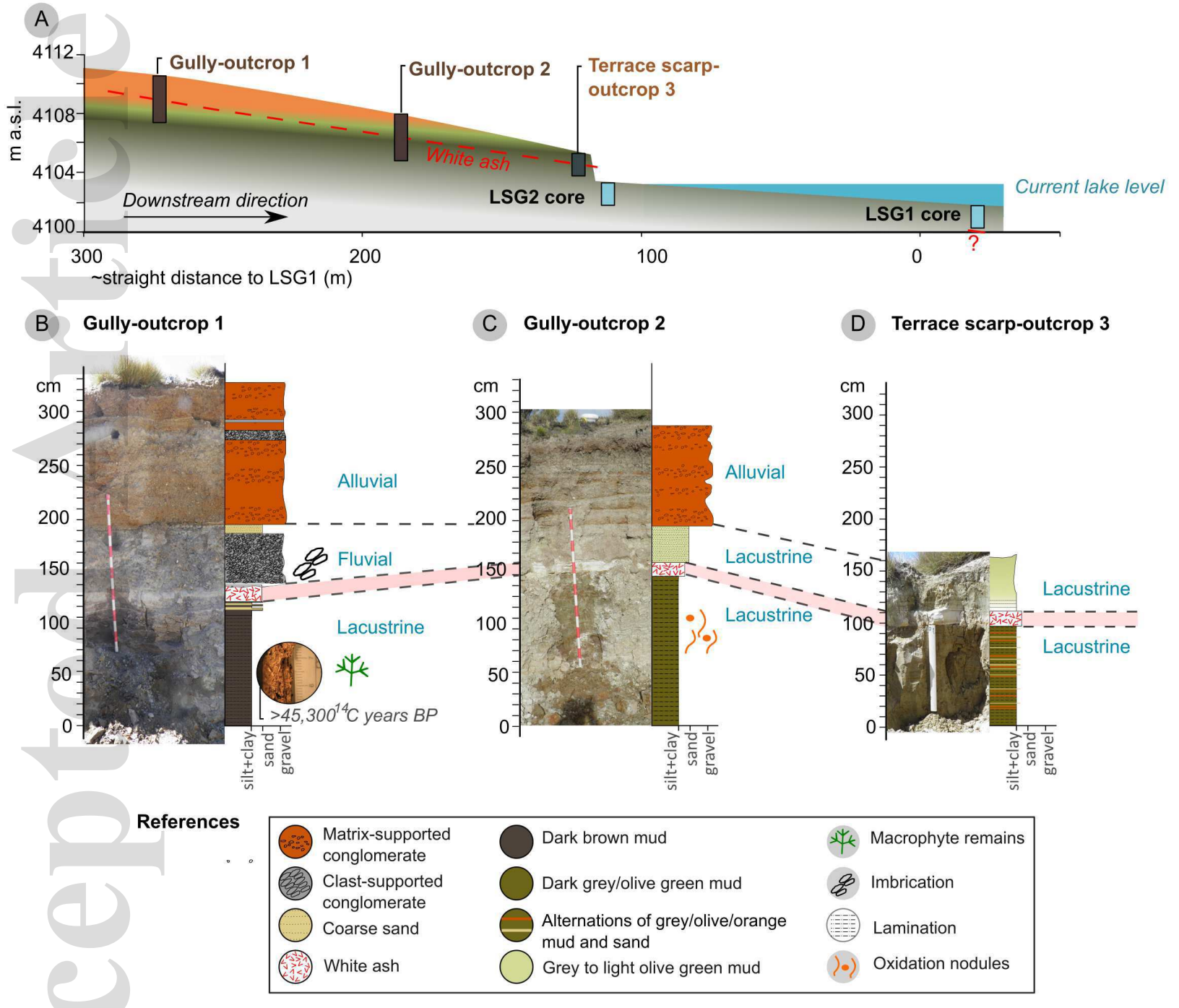

sed_13004_f3.eps

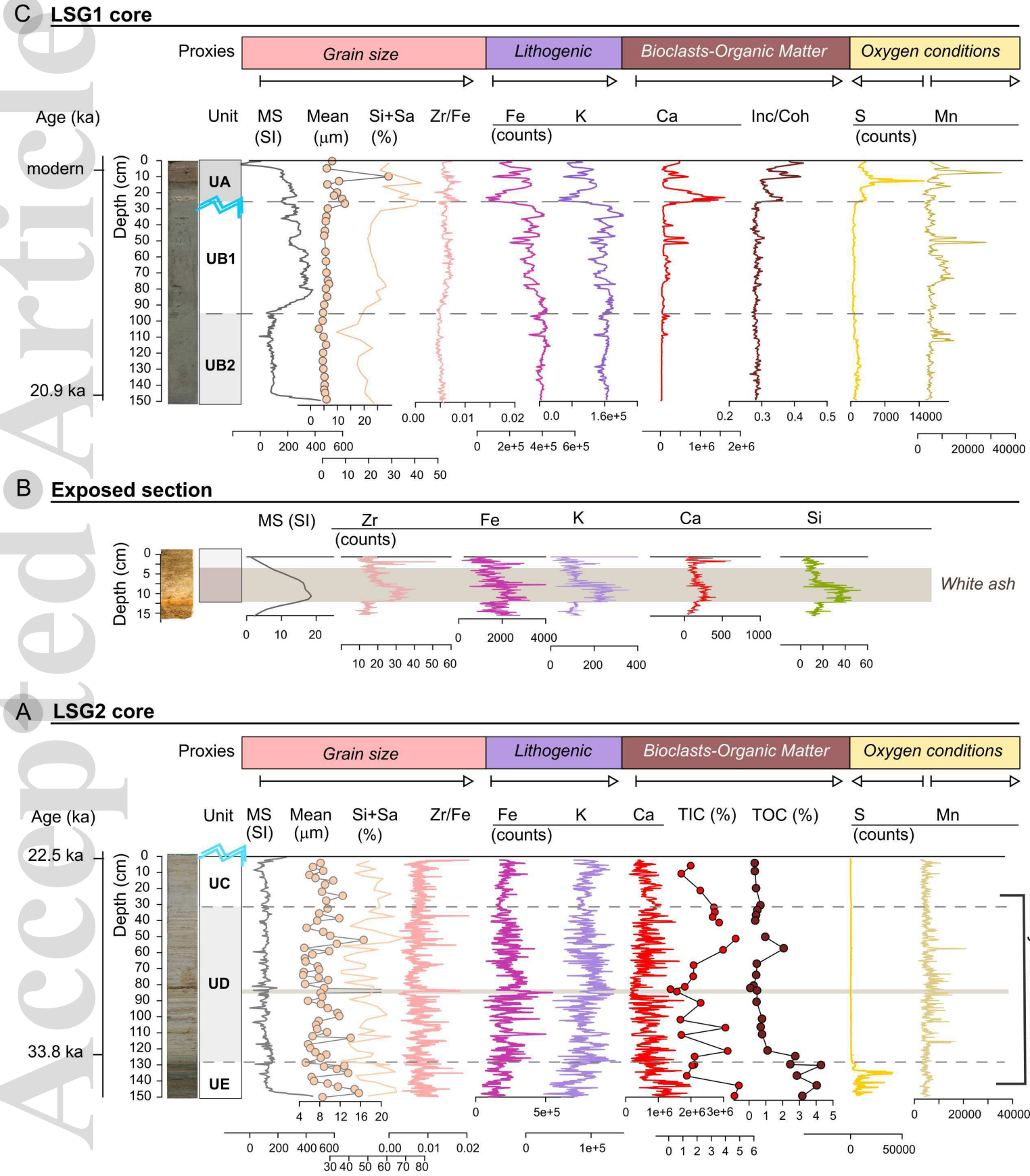

sed_13004_f4.eps

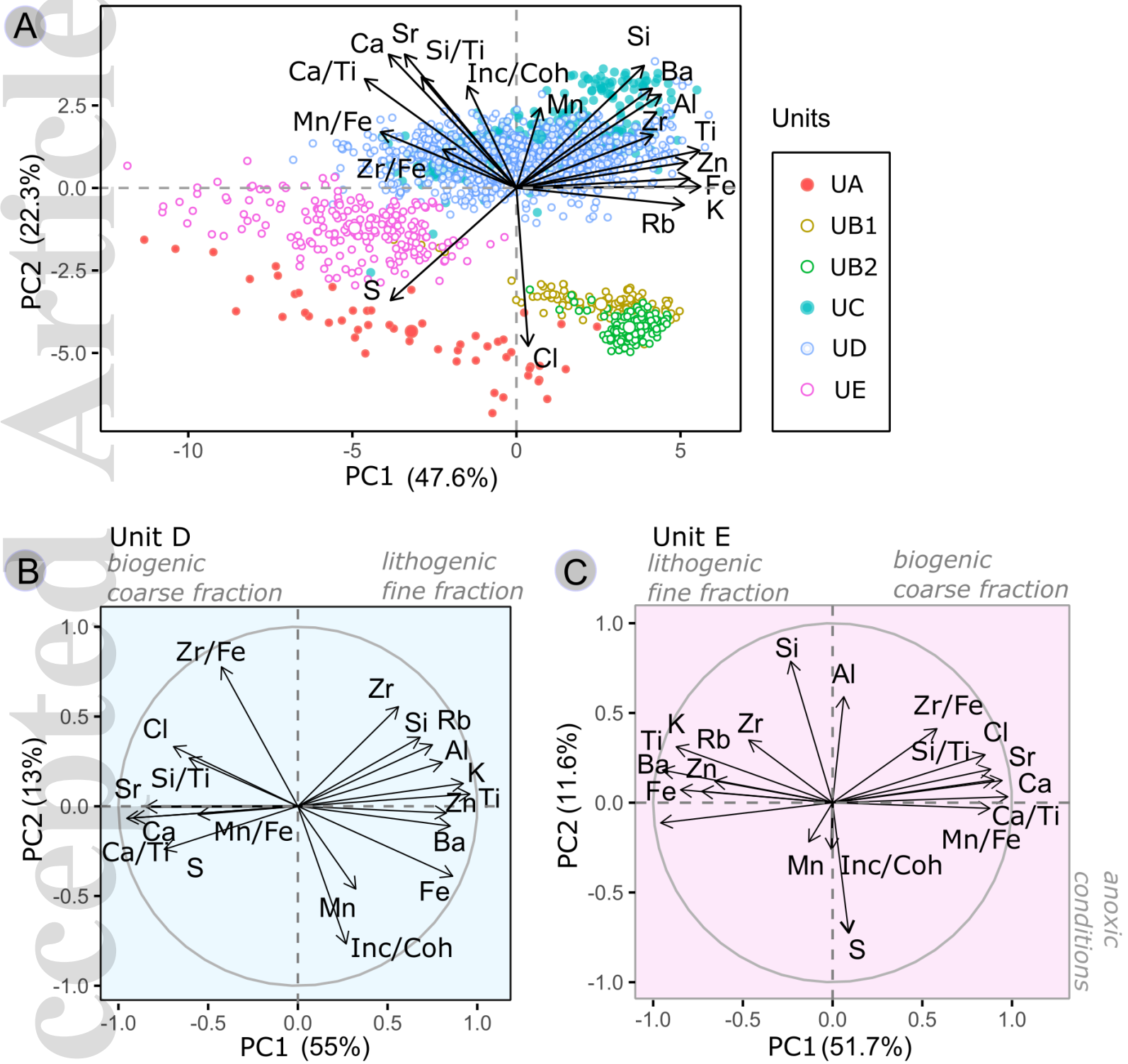

sed_13004_f5.eps

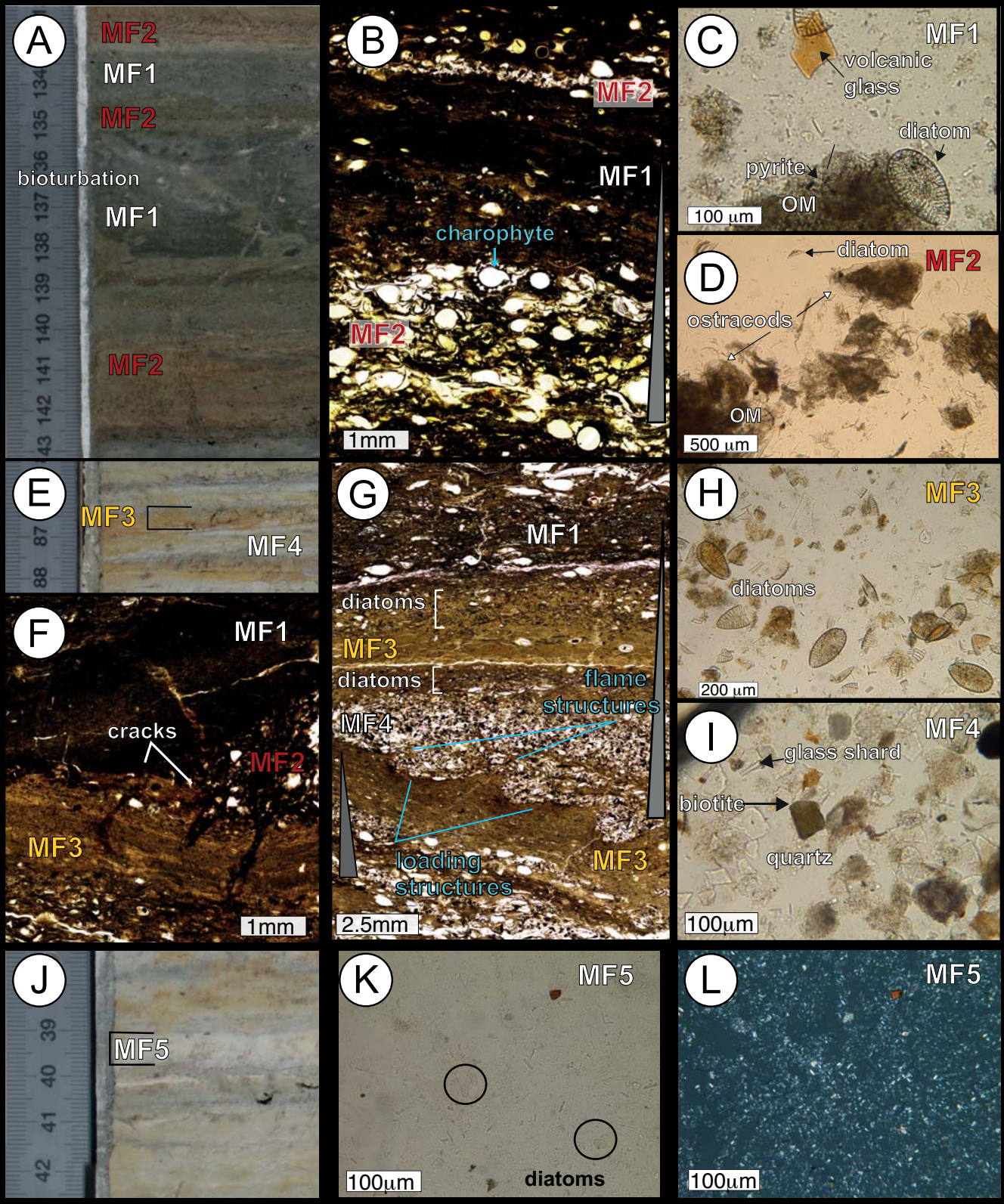
A
MF2
MF1
MF2
bioturbation
MF1
MF2
B
MF2
MF1
charophyte
MF2
1mm
C
MF1
volcanic glass
diatom
pyrite
OM
100 µm
D
diatom
MF2
ostracods
OM
500 µm
E
MF3
MF4
F
MF1
cracks
MF2
MF3
1mm
G
MF1
diatoms
MF3
diatoms
flame structures
MF4
loading structures
MF3
2.5mm
H
MF3
diatoms
200 µm
I
MF4
glass shard
biotite
quartz
100µm
J
MF5
K
MF5
100µm
diatoms
L
MF5
100µm

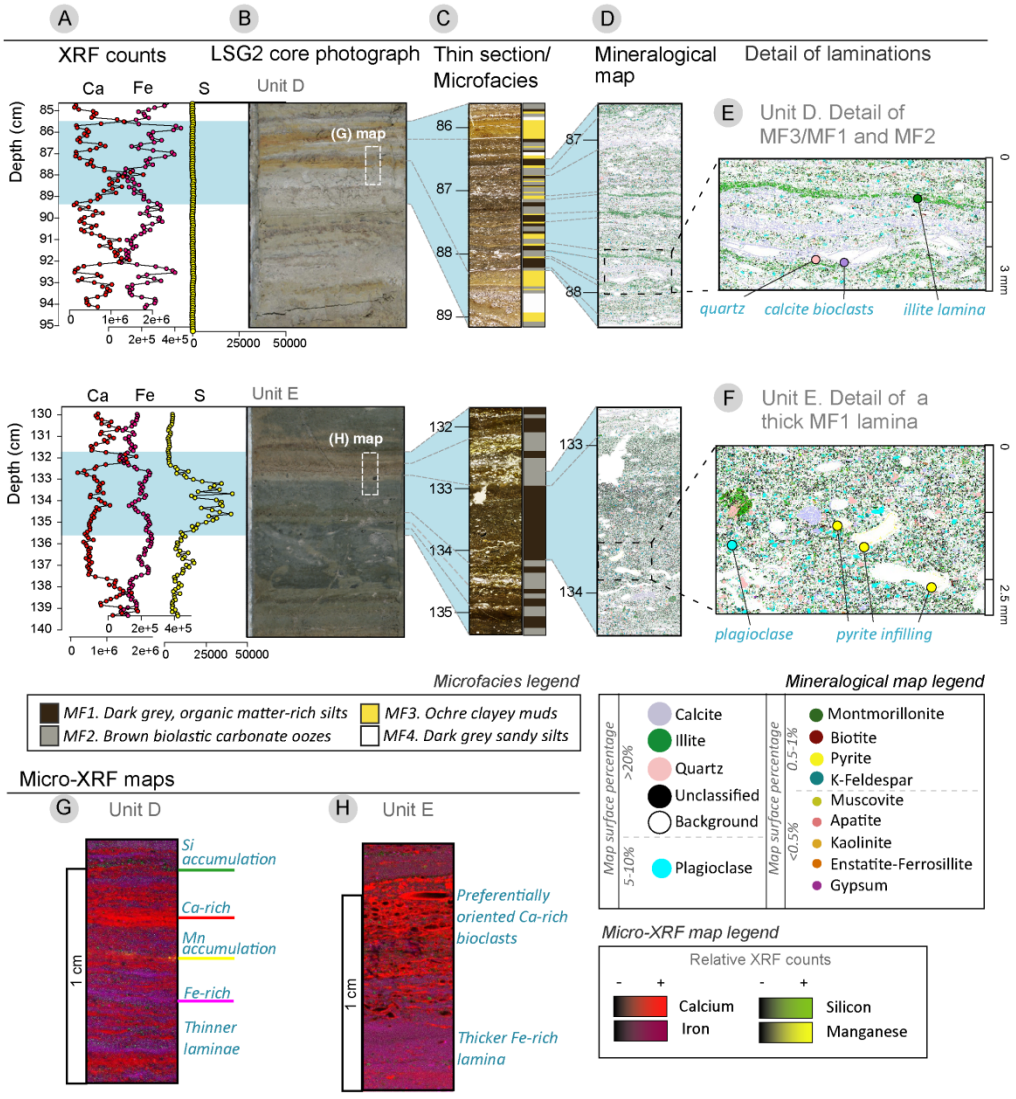

sed_13004_f7.tif

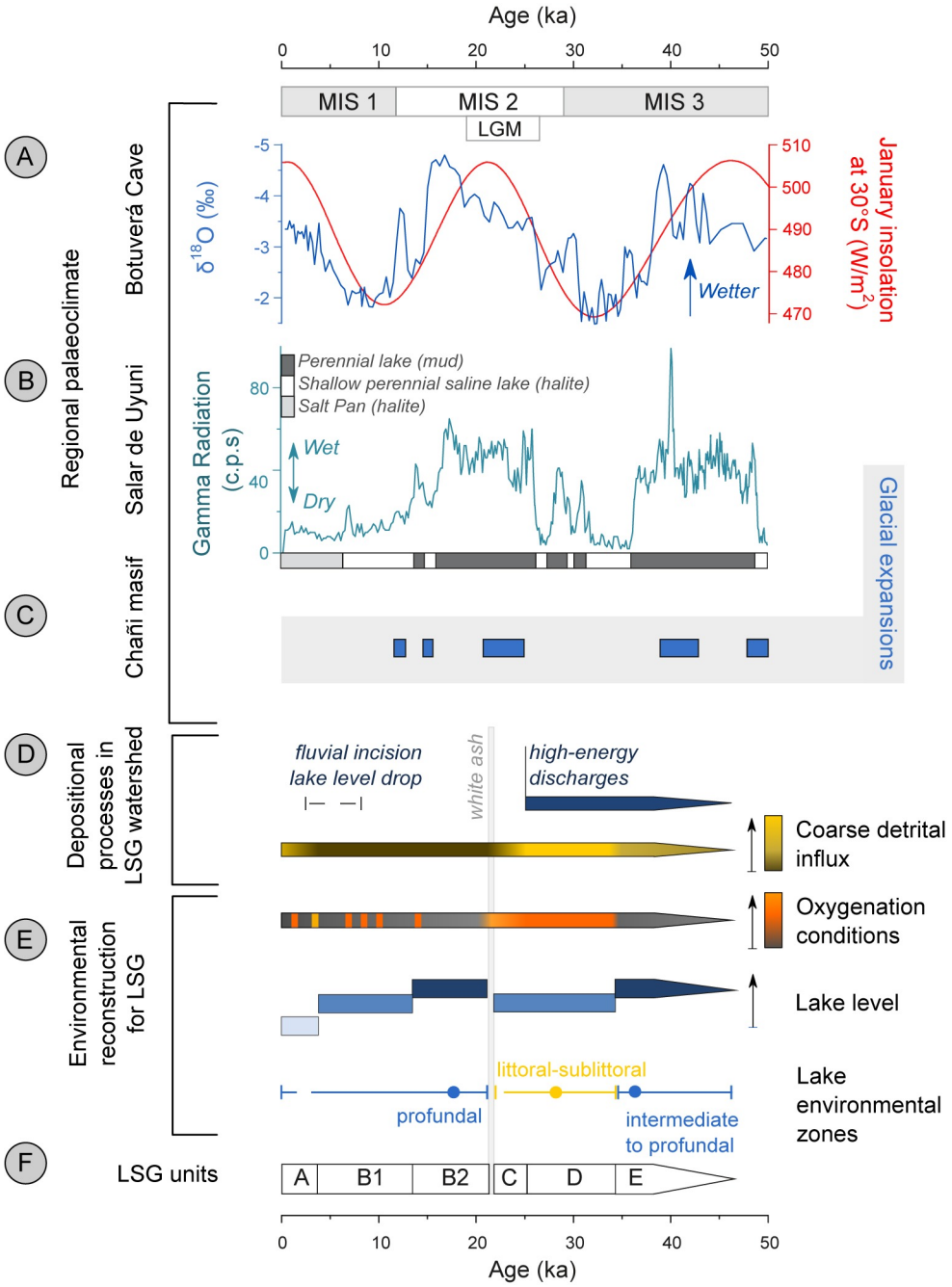

sed_13004_f8.tiff